Estimating $ZZ \to \ell\ell\nu\nu$ background in the $\ell\ell + E_T^{\text{miss}}$ final state using $Z\gamma \to \ell\ell\gamma$ data

A Thesis

submitted to
Indian Institue of Science Education and Research, Pune
in partial fulfillment of the requirements for the
BS-MS Dual Degree Programme

by

Mangesh Sonawane
Registration Number: 20121083

Indian Institute of Science Education and Research, Pune
Dr. Homi Bhabha Road,
Pashan, Pune 411008, INDIA

June 2017 - April 2018

Conducted at : DESY
Notkestraße 85,
22607, Hamburg
Germany

Supervisor: Dr. Beate Heinemann

Certificate

This is to certify that this dissertation, entitled "Estimating $ZZ \rightarrow \ell\ell\nu\nu$ background in the $\ell\ell + E_T^{\text{miss}}$ final state using $Z\gamma \rightarrow \ell\ell\gamma$ data", submitted towards the partial fulfilment of the BS-MS dual degree programme at the Indian Institute of Science Education and Research (IISER), Pune, represents the work carried out by Mangesh Sonawane at the Deutsches Elektronen-Synchrotron (DESY), Hamburg, under the supervision of Dr. Beate Heinemann, Professor of Experimental Particle Physics at the Institute of Physics, University of Freiburg, during the academic year 2017-2018.

Mangesh Sonawane

29.03.2018

Dr. Beate Heinemann

29.3.2018

Committee:
Dr. Beate Heinemann
Dr. Seema Sharma

I dedicate this thesis to my parents, Avinash and Ranjana Sonawane, my mentors, Dr. Sourabh Dube and Dr. Seema Sharma, and to my friends and colleagues and IISER, without whose timely advice and support this thesis would not have been made possible.

Declaration

I hereby declare that the matter containined in the thesis entitled "Estimating $ZZ \rightarrow \ell\ell\nu\nu$ background in the $\ell\ell + E_T^{\mathrm{miss}}$ final status using $Z\gamma \rightarrow \ell\ell\gamma$ data", contains the results of the work carried out by me at the Deutsches Elektronen-Synchrotron (DESY) Hamburg, under the supervision of Dr. Beate Heinemann, and the same has not been submitted elsewhere for any other degree.

Mangesh Sonawane

29 · 03 · 2018

Dr. Beate Heinemann

09.3.2018

Committee:
Dr. Beate Heinemann
Dr. Seema Sharma

Acknowledgements

Abstract

In the search for Dark Matter (DM) at the LHC, Standard Model particles are produced in association with Dark Matter particles, which are invisible as they do not interact with the detector. Thus events with large imbalance in transverse momentum are of interest. One such signature is $\ell\ell + E_T^{miss}$. The dominant background contributing to the search for Dark Matter in the $\ell\ell + E_T^{miss}$ is $ZZ \to \ell\ell\nu\nu$. Currently, this background is determined using Monte Carlo simulation, with an uncertainty of $\approx 10\%$. The goal of this study is to establish a data driven method to estimate this background, and reduce the uncertainty. Using $Z\gamma \to \ell\ell\gamma$, which is a process with low backgrounds and has a high $BR * \sigma$, it is possible to estimate the $ZZ \to \ell\ell\nu\nu$ contribution. In regions where $p_T(\gamma) \gg M_Z$, the two processes are kinematically similar. They have the same production mechanisms, but differ due to the couplings of the photon and Z boson to the quarks being different, as well as the difference in mass (photons are massless, while Z bosons are massive). Introducing a transfer factor R as the ratio $\sigma(ZZ)/\sigma(Z\gamma)$ which is determined from simulation, the contribution of $ZZ \to \ell\ell\nu\nu$ to the background can be estimated from $Z\gamma \to \ell\ell\gamma$ data. The uncertainty on the prediction of R due to theoretical aspects is estimated in this work.

Contents

List of Figures

List of Equations

List of Tables

Chapter 1

Introduction

Fundamental particle physics has a remarkable goal. It aims to explain the interactions of matter and energy with the minimum possible number of mathematical assumptions, with everything else in the universe being an emergent property.

Not only is it remarkably ambitious, the Standard Model, which describes the fundamental particles and their interactions [1], is one of the most successful theories developed. It is theoretically self-consistent, and has enjoyed tremendous success in providing accurate experimental predictions. However, the Standard Model is not a complete theory of fundamental interactions. It does not provide an explanation for several observed phenomena, such as gravity, or the accelerating expansion of the universe, among others.

One such question that triggers burning curiosity is the apparent incongruity of galaxy rotation curves with the theory of Newtonian mechanics: stars in the arms of spiral galaxies appear to move much faster than Newtonian physics would predict. Either the current understanding of mechanics is incomplete, or there is more mass present somewhere in the galaxy that is not visible by any method that is currently employed. This invisible hunk of matter is what is termed as Dark Matter (DM).

Detailed observations of these rotation curves, along with measurements of other phenomena such as gravitational lensing by distant galaxies, galaxy clusters, and Cosmic Microwave Background (CMB) lead to the conclusion that, if the Dark Matter hypothesis is true, the amount of visible Baryonic matter in the universe is a mere 4%. Dark Matter and Dark Energy make up the remaining 96% of the universe.

Now it becomes important to address the question: what exactly is Dark Matter?

Several extensions to the Standard Model, called Beyond Standard Model (BSM) theories, attempt to provide an explanation of these observed phenomena. Dark Matter has not been observed to interact directly through the electromagnetic force, and are thus invisible to current detectors. Consequently candidates particles for Dark Matter are called Weakly Interacting Massive Particles (WIMPs). In LHC experiments, events with WIMPs in the final state show up as an imbalance in the momentum in the plane transverse to the beam (referred to as E_T^{miss} throughout this thesis).

One such BSM theory postulates that these Dark Matter candidate particles may couple to Standard Model particles in interactions mediated by the Higgs boson. Fig 1.1 illustrates some of the possible processes for the production of the Higgs boson. The Higgs boson can then decay into invisible particles.

1
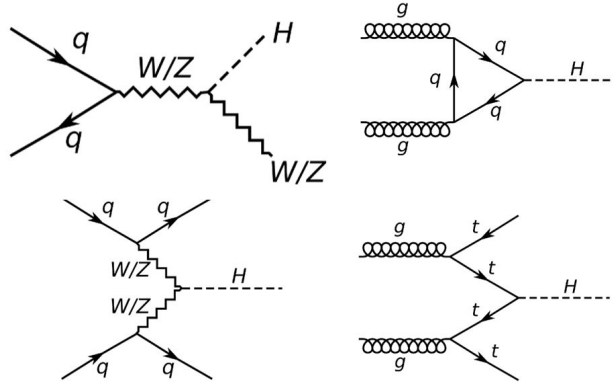
Figure 1.1: Feynman diagrams for the Standard Model production of the Higgs boson; VH: Higgs produced in association with a W/Z boson (top left), ggF: gluon-gluon fusion (top right), VBF: vector boson fusion (bottom left), ttH: (bottom right).

High energy collision experiments are a method to experimentally investigate the predictions made by particle physics in a controlled manner. Several other kinds of detector experiments, both passive and active, investigate phenomena such as neutrino flavor oscillations and direct dark matter searches. The Large Hadron Collider (LHC), built and operated by CERN, is a proton-proton (and heavy ion) collider located in Switzerland and France, is the largest such collider in the world. It has provided invaluable data since commencing operations in 2008, providing experimental confirmation for phenomena such as the Higgs boson.

In this thesis, a closer look is taken at the production of a Higgs boson in association with a Z boson, where the Higgs boson decays invisibly into Dark Matter particles, and the Z boson decays into a dilepton pair. The signature of such a process is two same flavor, oppositely charged leptons, and an imbalance in event momentum ($\ell\ell + E_T^{\mathrm{miss}}$). A possible search in this channel would constitute stacking all known Standard Model processes that contribute to the $\ell\ell + E_T^{\mathrm{miss}}$ signal (making up the background) and look for excesses in data which will indicate the presence of BSM processes. In this thesis, the $ZZ \to \ell\ell\nu\nu$ process is studied, which constitutes the dominant Standard Model background in the $\ell\ell + E_T^{\mathrm{miss}}$ final state. However, it is difficult to discriminate between the Standard Model $ZZ \to \ell\ell\nu\nu$ and $ZH \to \ell^+\ell^- + E_T^{miss}$, the process under consideration, because of the identical final state. Thus, an attempt is made to estimate it using alternate processes with clean signals.

This chapter gives an overview of the Standard Model, its constituent matter particles, forces, and their interactions. It also delves into the shortcomings of the Standard Model, and introduces some ways in which Dark Matter is probed at the LHC. Chapter 2 describes the LHC, as well the ATLAS detector, where high energy collisions experiments are carried out. Chapter 3 discusses the theoretical aspects of investigating the $ZZ \to \ell\ell\nu\nu$ contribution, and details the approach taken, and chapter 4 presents the results obtained.

1.1 The Standard Model

The Standard Model is the theory of particles, fundamental forces, and interactions that govern the universe. It describes three of the four forces: the electromagnetic, strong and weak forces. The Standard Model is formulated using the framework of Quantum Field Theories (QFT), which describe particles as excitations of an underlying field.

Throughout this thesis, the Lorentz-Heaviside system of units is used, such that $c = \hbar = 1$ (where c is the speed of light, and $\hbar = h/2\pi$ is the reduced Planck's constant), and thus these units do not show

2

63 up in equations. Ref [1] is the reference textbook for much of this section.

1.1.1 Matter and Forces

65 In the Standard Model, matter is made up of fermions and bosons. Fermions are particles with half-
66 integer spin, and interact through the exchange of gauge bosons, which have integer spin. All fun-
67 damental Standard Model fermions have spin 1/2. The Standard Model gauge bosons which mediate
68 the interactions between particles have spin 1. The Higgs boson is a scalar boson, and has spin 0.

69 Figure 1.2 shows a schematic representation of the elementary particles in the Standard Model.
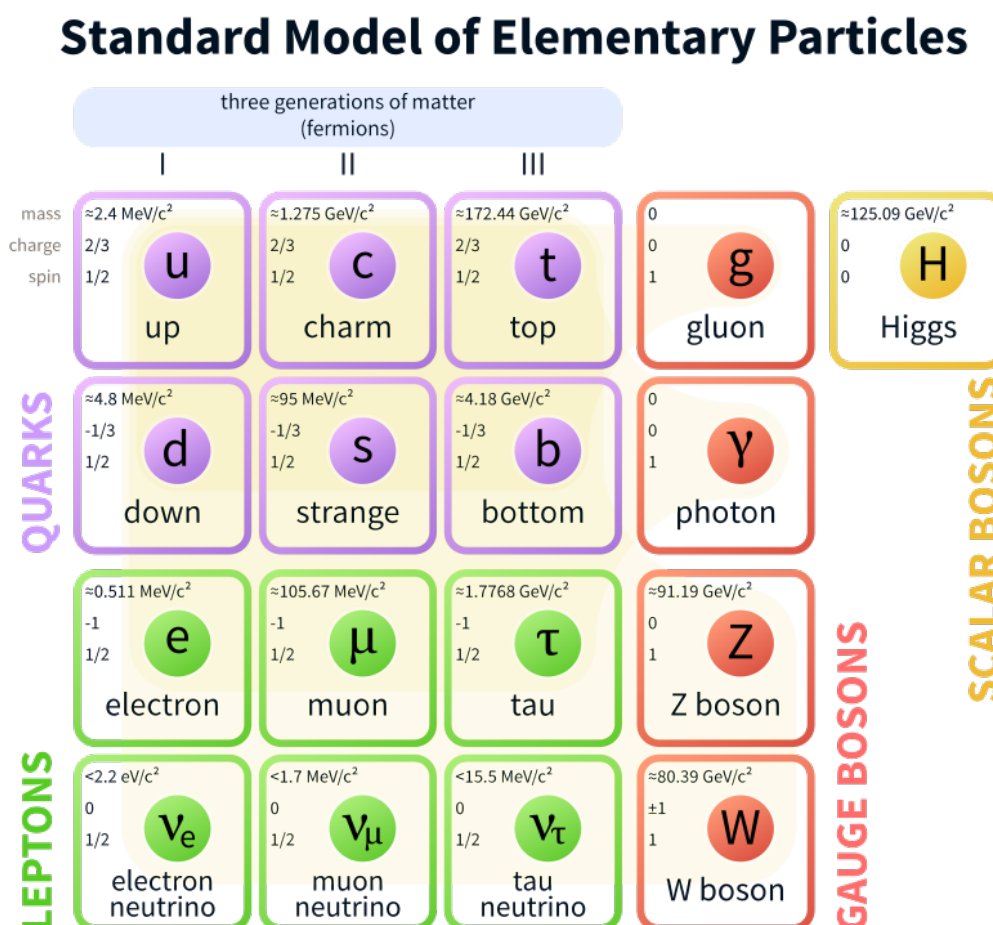
Figure 1.2: A schematic representation of the Standard Model [2] of particles. The table shows the
three generations of fermions (classified as quarks and leptons) that make up all known matter in the
universe, and bosons that mediate interactions, and are thus responsible for 'forces'.

70 All particles, except the neutral bosons (with no electromagnetic charge) have a corresponding an-
71 tiparticle, which has the same properties, except with an opposite electric charge.

72 Fermions are divided into two categories: leptons and quarks. There are six flavors of leptons and
73 six flavors of quarks. All the quarks, and three flavors of leptons are electrically charged, and thus
74 participate in electromagnetic interactions. Electromagnetic interactions are described by **Quantum**
75 **Electrodynamics** (QED) [3], a QFT. QED describes interactions in which two electrically charged
76 particles exchange a photon. The photon is a spin-1 gauge boson, is electrically neutral, massless, and
77 mediates electromagnetic interactions. Figure 1.3 shows the fundamental interaction vertex in QED,

the interaction between two charged fermions and the photon.
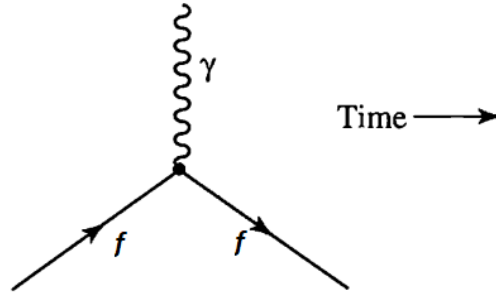
Figure 1.3: Feynman diagram showing the fundamental interaction vertex in Quantum Electrodynamics. Charged fermions (f) interact via the exchange of a photon (γ), reproduced from Ref [1].

Quarks come in 6 flavors, which are divided into 3 'generations' having progressively higher masses; the up and down (u and d) are first generation quarks, charmed and strange (c and s) are second generation quarks, top and bottom, or formerly, truth and beauty, (t and b) belong to the third geneeration. Up-type quarks (u, c and t) have an electric charge of +2/3e (where e is the unit of electronic charge, equal to 1.6×10^{-19} Coulombs), while down-type quarks have an electric charge of -1/3e. Quarks are the fundamental particle that form composite particles called hadrons; bound states of $q\bar{q}'$ are called *mesons*, and $qq'q''$ bound states are called baryons. Protons (bound state of uud) and neutrons (bound state of udd) are the most familiar examples of baryons.

Hadrons are bound together by the strong nuclear force. The strong interaction is described by the theory of **Quantum Chromodynamics** (QCD). In QCD, the strong interaction is mediated by gluons, which, like the photon, are massless spin-1 gauge bosons. However, unlike the photon, gluons do not carry electric charge. Instead, they carry an analogous color charge. There are three types of color charge, dubbed "red", "green" and "blue". These titles are arbitrary, and have been chosen under the heuristic that all naturally occurring states must be "colorless". Thus, a baryon must have three quarks such that red, green and blue occur in equal measures, or meson must have a quark and antiquark such that the color and anticolor cancel out. This leads to the implication that a color charged object cannot exist in isolation, a phenomenon known as confinement [4].

Quarks interact through the strong force, and they are the only fermions to do so. Quarks, like gluons, carry color charge and can interact with gluons. Gluons have several interesting properties; they are massless, have no distinct antiparticle, and are capable of self interaction, as shown in Figure 1.4. These properties lead to gluons splitting and radiating infinitely. Such interactions occurring in the vicinity of quarks result in the strength of the strong force changing inversely as a function of the distance between interacting quarks, i.e. quarks that are close to each other interact less strongly than quarks that are further apart. When quarks are separated, the potential energy arising from the strong force increases until it is energetically more favorable for the production of a quark-antiquark pair from the vacuum, screening the quarks, than it is to maintain the separation between them. This process, where a color-charged particle will cause other color-charged particles to be produced from the vacuum until the resulting bound state is color-neutral, is known as *hadronization*, and results in single quarks or gluons from the hard interaction point forming "jets" of several hadrons in the detector.

Confinement explains why isolated quarks or gluons have never been observed, and why the strong-interaction is short ranged despite being mediated by the massless gluons. The property of strongly interacting particles, that at small distances of the order of less than a femtometer they basically act as free particles, is known as *asymptotic freedom*. At these scales, quarks and gluons may be treated individually rather than as a bound state.

4
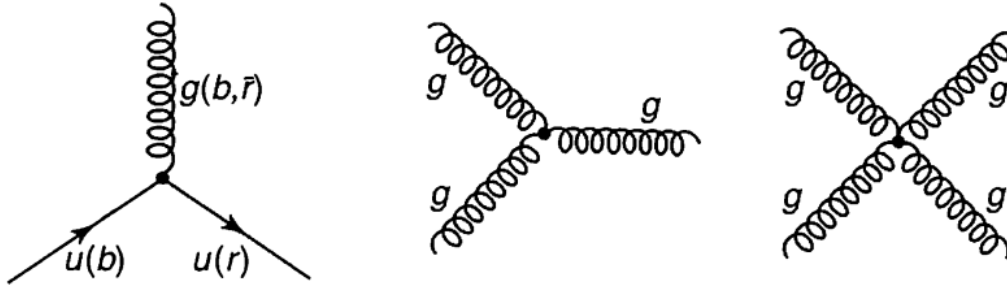
Figure 1.4: Feynman diagram showing the fundamental interaction vertex in Quantum Chromodynamics. reproduced from Ref [1]. The quark-quark-gluon vertex (left) shows the gluon mediating the interaction between two *up* quarks, with their color content visible, to illustrate the conservation of color charge. Gluons are also capable of self-interacting, leading to three- or four-gluon interaction vertices (center, right).

The other family of fermions, leptons, also form three generations. Each generation consists of an electrically charged lepton, and its corresponding electrically neutral neutrino; i.e. electrons (*e*), muons (μ) and taus (τ) (in increasing order of mass), which have an electric charge of -1*e*, and their correspondingly flavored neutrinos (ν_e, ν_μ and ν_τ). Neutrinos, assumed by the Standard Model to be massless, have been observed to oscillate between flavors [5–7], implying that they have small masses, but which have not been measured. Tau leptons are the heaviest at 1.78 GeV, and decay rapidly, having a mean lifetime of 2.9×10^{-13} s in their rest frame. Muons have a mass of 106 MeV, about 200 times heavier than that of the electrons (0.511 MeV). Muons, however, decay with a mean lifetime of 2.2μs, which is long compared to the time scales in collider experiments, and are stable enough to pass through the detectors intact.

All leptons interact through the weak nuclear force. As neutrinos have no electric charge, they only participate in Standard Model interactions through the weak interaction, thus making them difficult to detect. Collider experiments do not even attempt to detect neutrinos. Instead, their presence is inferred through momentum imbalance (as they are invisible to the detectors).

There are two kinds of weak interactions; charged-current and neutral-current interactions. The Z boson, an electrically neutral, spin-1, massive gauge boson, mediate neutral-current weak interactions. Such interactions are analogous to electromagnetic interactions. However, there are notable differences. The Z boson is massive (having a mass of 91 GeV), whereas the photon is massless. This limits the range of the interaction, as the Z boson decays, and has a mean lifetime of the order 10^{-25}s. The fact that the Z boson is massive gives it longitudinal polarization modes [8] as well, which the photon does not possess. The Z boson also mediates interactions between neutrinos, which the photon does not as neutrinos are electrically neutral. Also, weak interactions do not respect Parity (P) symmetry. The coupling strengths of the Z boson to fermions depends on their flavor and helicity, with left-handed fermions and right-handed anti-fermions coupling more strongly than right-handed fermions and left-handed anti-fermions. In fact, the Z boson does not couple at all to right-handed neutrinos. However, neutral-current interactions still respect combined charge and parity (CP) symmetry.

A slight digression to define helicity is warranted at this point. Helicity is defined as the projection of a particle's spin vector onto its momentum vector. If the helicity is positive, the particle is considered to be right-handed. If it is negative, the particle is considered to be left-handed.

Charged-current interactions are mediated by the W^+ and W^- bosons, which carry an electrical charge. Charged-current interactions do not respect parity symmetry either, and are in fact maximally parity violating; the W bosons only couple to left-handed fermions and right-handed anti-fermions. Therefore, as neutrinos only interact weakly, and neither the Z nor W bosons interact with right-handed neutrinos, there does not appear to be a reason for right-handed neutrinos to exist within

the Standard Model. Charged-interactions do no respect the combined CP symmetry either, unlike neutral-current interactions. This CP violation occurs at a small but measurable rate. The first evidence of CP violation was provided by the Fitch-Cronin experiment [9], in 1964, in the neutral kaon system, before the theory of the weak force was even completely formulated. After its formulation, it was apparent that CP violations arise from a complex phase in Cabibbo-Kobayashi-Maskawa (CKM) matrix [10], a unitary 3×3 matrix shown in Figure 1.5. Charged-current weak interactions are capable of coupling quarks from different generations, the degree of which is given by the CKM matrix. A complex phase in the elements of this matrix is what gives rise to CP violation.

$$\begin{bmatrix} d' \\ s' \\ b' \end{bmatrix} = \begin{bmatrix} V_{ud} & V_{us} & V_{ub} \\ V_{cd} & V_{cs} & V_{cb} \\ V_{td} & V_{ts} & V_{tb} \end{bmatrix} \begin{bmatrix} d \\ s \\ b \end{bmatrix}$$

Figure 1.5: The Cabibbo-Kobayashi-Maskawa matrix that shows the degree of mixing among the quark flavors. Charged-current weak interactions, mediated by the W bosons, allow coupling of quarks between two generations, causing the eigenstates of the weak interaction d', s' and b' to be superpositions of the observable mass eigenstates d, s and b.

CP violation has subsequently been confirmed in several meson decays [11–16].

Continuing the analogy between the electric charge and the color charge to the weak interaction as well, the quantum number for the weak interaction is the three-component weak isospin, T^i. It is typically defined such that T^3 is the measure component, and may be treated as the weak charge. Weak isospin is conserved in electromagnetic, strong and fermion-fermion weak interactions, however interactions involving the Higgs field change this isospin of particles. Electric charge Q, however, is always conserved, and is described in terms of the weak isospin T^3 and the weak hypercharge (the quantum number corresponding to the $U(1)$ gauge symmetry) Y_W.

$$Q = T^3 + \frac{1}{2} Y_W$$

The connection between the electromagnetic and weak forces, and the similarities between weak neutral-current interactions and QED hint at unification, and indeed the Standard Model unifies the them into a single *electroweak* force. The differences between electromagnetic and weak interactions, such as the mass of weak gauge bosons, arise from electroweak symmetry breaking.

The strong, weak and electromagnetic forces can be described by the $SU(3) \times SU(2) \times U(1)$ local gauge symmetry group, where the $SU(3)$ symmetry group describes the strong interaction, and the electroweak interactions are based on the $SU(2) \times U(1)$ symmetry group. There are 8+3+1 generators associated with this model, each generator corresponding to a vector boson. Thus, there exist 8 gluons for the 8 generators of the $SU(3)$ group. The interaction of the scalar Higgs field with the vector fields W^+, W^-, W^0 and B causes the spontaneous breaking of the $SU(2) \times U(1)$ symmetry, resulting in 3 massive and one massless gauge boson. It also implies the existence of a neutral scalar boson, known as the Higgs boson, which was discovered in July 2012 [17, 18]. The 3+1 generators of $SU(2) \times U(1)$ correspond to the W^+, W^- and Z bosons, massive vector bosons , and the massless vector boson γ (photon).

Vertices in Feynman diagrams, such as in Figures 1.3 and 1.4, correspond to a coupling between the particles, which is quantified by a coupling constant. The coupling constant in electromagnetic interactions is called the fine structure constant α. It is a dimensionless constant, and arises from the ratio of the interaction energy between two electrically charged particles to the energy of a photon, and is approximately equal to 1/137. In strong interactions, this coupling is denoted by α_S, and is very

different from the electromagnetic coupling constant. The strong coupling α_S changes as a function of distance (or equivalently, the energy scale of the interaction), with it having a larger magnitude at larger distances (small interaction energy scales), and is small at distances smaller than a nucleon (high interaction energy scales), leading to strongly interacting particles behaving as though they are free; the origin of asymptotic freedom. This scale dependence is known as the running of the strong coupling constant. The value of the strong coupling constant at lengths scales of about the separation of nucleons ($\approx 10^{-15}$ m) is ≈ 1. The weak interaction has an extremely short range. Thus the weak coupling constant, evaluated from the lifetime of a muon, and has a coupling of strength of between $10^{-7} - 10^{-6}$. Thus, at length scales of the order of femtometers (10^{-15} m), the electromagnetic, weak and strong coupling strengths are in the ratio (up to the closest order of magnitude) $10^{-2} : 10^{-6} : 1$. The strong coupling α_S is small at high interaction energy scales due to asymptotic freedom, and thus processes that occur at such energies may be calculated perturbatively, in a framework called perturbative QCD (pQCD).

Predictions in pQCD are made in terms of the renormalized coupling $\alpha_S(\mu_R^2)$. When μ_R is taken to be close to the momentum transfer scale Q of a process, the strong coupling constant $\alpha_S(\mu_R^2 \simeq Q^2)$ indicates the strength of the strong interaction in the process. Renormalization is required to address low and high energy divergences (infrared, IR, and ultraviolet, UV, divergences respectively). μ_R and μ_F are the renormalization and factorization scales, arbitrary and unphysical parameters used to absorb the effects of the UV and IR divergences respectively. Renormalization is briefly discussed in Section 3.6

The strong coupling satisfies the following renormalization group equation (RGE):

$$\mu_R^2 \frac{\mathrm{d}\alpha_S}{\mathrm{d}\mu_R^2} = \beta(\alpha_S) = -(b_0\alpha_S^2 + b_1\alpha_S^3 + b_2\alpha_S^4 + ...) \tag{1.1}$$

where the b_i are the loop-coefficients of the coupling α_S, and μ_R is the renomalization scale, of which α_S is a function. The minus sign on the right hand side of Equation 1.1 dictates that the strong coupling constant becomes small for processes involving large momentum transfers, and is the source of asymptotic freedom. For such processes, α_S is sufficiently small to be treated perturbatively, and this theoretical framework is called perturbative QCD (pQCD). Calculations for most processes occurring at high momentum transfer scales can be simplified by only calculating up to a fixed order.

Each interaction vertex in a Feynman diagram translates to a term featuring the corresponding coupling constant in the transition amplitude of the process from initial state to final state. The order of a coupling constant in a process is the number of times the vertex features in the transition amplitude i.e. a process having two strong vertices can be described as $O(\alpha_S^2)$. For interactions that take place at low interaction energies, the electromagnetic and weak coupling constants are much smaller than one. Thus, Feyman diagrams with more weak or electromagnetic vertices contribute less than lower order diagrams, and may be treated perturbatively. Higher order Feynman diagrams with strong vertices, however, must be at high interaction energies to be treated perturbatively. In perturbative expansions, the term with the highest contribution is known as the leading order (LO) term; the term with the next highest contribution is called the next-to-leading order (NLO) term, and so on.

Considering that the electromagnetic and weak forces have been unified into the electroweak force, it is speculated that there exists an energy scale where all the coupling constants are expected to be identical. This idea of the unifying all the forces at some scale known as the "Grand Unification" scale is unproven as of now, and the value of this scale is not known. In perturbative QFT, often divergences are encountered when calculating the cross section. To remove these divergences, terms dependent on the momentum scale of the interactions are introduced. The coupling constants then depend on this scale as well.

1.2 Inadequacies of the Standard Model

Despite its immense success, the Standard Model does not paint a complete picture of everything that we observe. It does not account for several phenomena that are experimentally observed, such as:

- Dark Matter and Dark Energy: Cosmological observations, such as galaxy rotation curves, do not match predictions based on the visible amount of mass in the universe. A fit with the observations predicts additional invisible matter, called Dark Matter [19]. Similarly, the universe is expanding at an accelerating rate, which hints at the existence of Dark Energy [20]. The Standard Model does not account for exotic matter such as these. In fact, the Standard Model only accounts for about 4% of the content of the universe [21, 22].

- Hierarchy problem [23–26]: Quantum corrections to the Higgs boson mass are divergent, and force it to be very large. However, the ATLAS and CMS collaborations measured the Higgs boson mass to be rather light, at 125 GeV [17, 18]. There appear to be some extraordinary fine tuned cancellations that make this mass so small.

- Matter-antimatter asymmetry: Matter and antimatter should have been created in equal quantities at the moment of the Big Bang. However, the universe appears to be almost completely made out of matter, indicating that in the initial state of the universe, this symmetry was broken [27].

- Neutrino masses: In the Standard Model, neutrinos are assumed to be massless. However, neutrino oscillations have been observed [28], which are only possible if neutrinos have mass [29].

- Gravity: The Standard Model is incompatible with general relativity [30]. It does not provide an explanation for gravity.

The Standard Model is incomplete, and thus requires modifications or additions to it, which are collectively called Beyond Standard Model (BSM) theories.

1.2.1 Dark Matter

Cosmological observations of galaxies made over the decades, such as the velocity curves of galaxies (called galaxy rotation curves) indicate an anomaly; the stars in the arms of spiral galaxies appear to move faster than what would be expected from Keplerian relations, using the visible mass from the galaxies. Figure 1.6 shows the two rotation curves, expected and observed, of NGC 6503, a field[1] spiral galaxy. [31]

---

[1]Field galaxies do not belong to a large cluster, and are thus gravitationally isolated
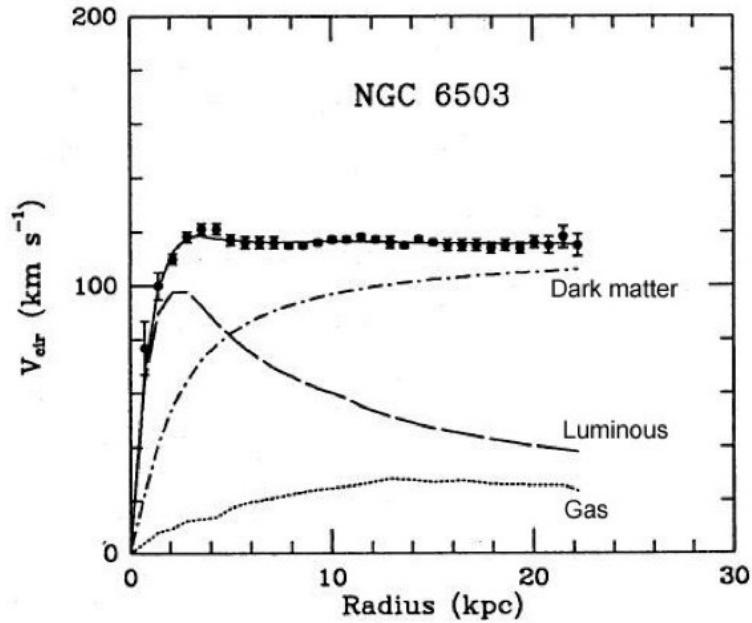
Figure 1.6: Velocity of stars in NGC 6503, a field spiral galaxy, as a function of radial distance from the center of the galaxy [31]. The 'Luminous' curve is what would be expected from the visible mass, but what is observed is much higher, indicating excess invisible matter.

Either the current understanding of Newtonian Mechanics is incomplete, or there is additional mass that is not visible which is contributing to the mass term in Newton's equation. This invisible mass is what is termed as Dark Matter. Ergo, Dark Matter appears to interact gravitationally, but not electromagnetically, with visible (Standard Model) matter. It is possible that Dark Matter is made up of and exotic and hitherto undiscovered kind of matter, and searches are underway at the LHC to look for Dark Matter via its interactions with the Standard Model.

There is additional cosmological evidence supporting Dark Matter, such as gravitational lensing of distant galaxies, structure formation in the early universe, anisotropy in the cosmic microwave background, etc.

1.2.2 Beyond the Standard Model

Several extensions to the Standard Model have been proposed that attempt to address some of its inadequacies.

Supersymmetry (SUSY) adds another symmetry to the Standard Model, predicting the existence of *supersymmetric* partners called sparticles, to Standard Model particles. For example, sleptons are supersymmetric partners to the corresponding leptons, and differ by spin 1/2. SUSY would also resolve the hierarchy problem by ensuring that the divergences would cancel out at all orders in the perturbation expansions, if the superpartners have mass near the electroweak scale (broadly, between 100 and 1000 GeV).

The observation of neutrino oscillations implies that neutrinos have mass, however, these observations can only reveal the mass difference between the different neutrino flavors. The absolute mass of the neutrinos has been constrained to have an upper limit of 2 eV, much smaller than the lightest Standard Model particles, by precision measurements of tritium decays. To incorporate neutrino masses, an extension to the Standard Model, the see-saw mechanism, introduces right handed neutrinos and couples them to left-handed neutrinos with a Dirac mass term.

9

Both SUSY and the addition of a sterile right-handed neutrino to the Standard Model are extensions that could provide possible candidates for Dark Matter. These candidates are known as Weakly Interacting Massive Particles (WIMPs). They do not interact electromagnetically, and are thus invisible to most detectors.

BSM theories propose experimental predictions which, if observed, could confirm that Dark Matter does exist and provide insight into its nature and properties.

Dark Matter searches at the Large Hadron Collider

As Dark Matter does not interact electromagnetically, any Dark Matter particles produced in collider experiments will be invisible to detectors at the LHC. Thus, in event reconstruction, such events are expected to be marked by a significant imbalance in transverse momentum (E_T^{miss}). Currently, Dark Matter searches are conducted at the LHC [32]. Dark Matter particles are denoted by χ.

Among the Dark Matter signature searched for at the LHC, E_T^{miss} +X is an important signature. These searches look for the production of a Standard Model particle in association with E_T^{miss}. Figure 1.7 shows the Feynman diagrams for the E_T^{miss} +X processes. The requirement of Dark Matter to be produced in association with another particle is imposed so that the event signature is identifiable, and allows the events to be triggered upon.

- E_T^{miss} +jet : In theory, it is possible to produce Dark Matter particles in association with one or more QCD jets from initial state radiation. Thus E_T^{miss} +jet searches look for one or more jets in events with large E_T^{miss} .

- E_T^{miss} +V : In a similar manner to E_T^{miss} +jet searches, a E_T^{miss} +V search looks for a single vector (γ, W or Z) boson. If Dark Matter particles couple directly to a pair of gauge bosons, this may be the dominant mode of Dark Matter production.

- E_T^{miss} +Higgs : It may also be that a single Higgs boson is produced in association with E_T^{miss} . Such events would be characterised by a $H \to \gamma\gamma$ or $H \to bb$ final state.
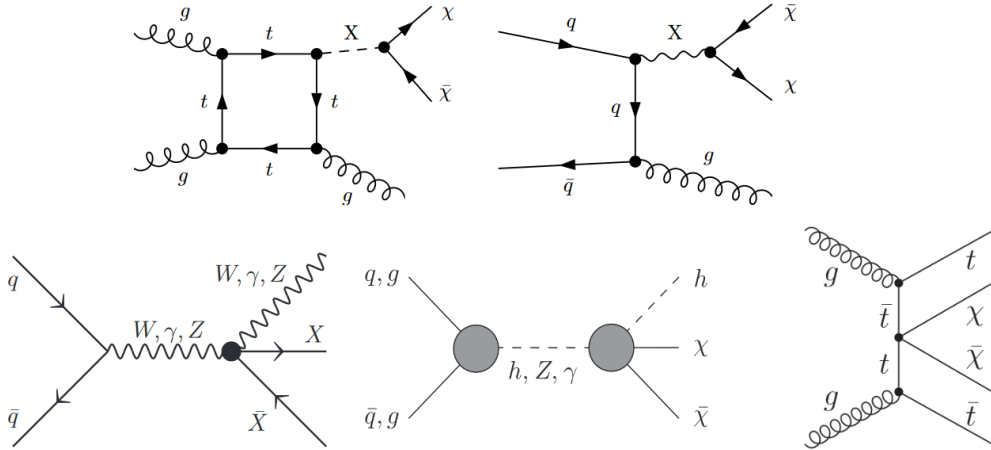
Figure 1.7: Feynman diagrams for mono X processes, showing E_T^{miss} +jet production (top) induced by gluons (top left) and quarks (top right) [33] where the mediator X can be a scalar, pseudo-scalar, vector or axial-vector particle; E_T^{miss} +V (bottom left) [34]; and E_T^{miss} +higgs (bottom center) [35], where h is the Standard Model Higgs boson with mass 125 GeV; gluon-induced $t\bar{t}+E_T^{\mathrm{miss}}$ (bottom right)

- E_T^{miss} +top : If Dark Matter particles couple predominantly to heavy quark flavors, a search for a top quark pair is a promising direction to head in.

- E_T^{miss} +VBF : In such events, Dark Matter particles are produced from a vector boson fusion.

Several models propose mediators that couple Dark Matter particles to Standard Model particles. These mediators can be vector, pseudo-vectors, scalars, pseudo-scalars or axions. The Higgs boson is an example of a scalar mediator, and is what this thesis focuses on.

Models using the Higgs as a mediator result in events with the Invisible Higgs signature; if the mass of the Dark Matter particles is less than half the mass of the Higgs boson, it may be possible that the Dark Matter particles couple to the Standard Model via the Higgs boson, i.e $H \to \chi\chi$ processes. The main methods of Standard Model Higgs production are shown in Figure 1.1.

- Vector boson fusion (VBF): In VBF processes, the Higgs is produced from the interaction of two vector bosons.

- Production of Higgs in association with a massive vector boson (VH) : This mechanism, together with VBF are the most important methods of Higgs production in invisible Higgs searches. Such events can be recognised with a large imbalance in transverse momentum, as well as the decay products of the vector boson.

- Gluon gluon fusion (ggF) : It is also possible for the Higgs to be produced from the interaction of gluons. This is similar to a E_T^{miss} +jet like search.

Chapter 2

Experimental Apparatus

2.1 The Large Hadron Collider

The Large Hadron Collider (LHC) is a circular particle collider located in France and Switzerland. It was built by the European Council for Nuclear Research (CERN) in collaboration with over 10000 scientists from all over the world, between 1998 to 2008, when it began its operation and started collecting data. It is the world's largest, most powerful particle collider, focusing primarily on proton-proton collisions, but also conducts heavy ion collision experiments.

The goal of the LHC is to experimentally test predictions made by theories of particle physics, and look for evidence of new physics. It has enjoyed remarkable successes, such as the discovery of the Higgs Boson in 2012 [17, 18].

The LHC houses seven experiment. ATLAS and CMS are the largest, general-purpose detectors that research a number of Standard Model predictions, such searches for new physics and measurements of Standard Model parameters, among other tasks. ALICE is a heavy ion collider experiment that studies lead-lead collision, while LHCb studies mesons and baryons containing b- or c- quarks. In addition, three smaller experiments, TOTEM, MoEDAL and LHCf, are used for highly specialized research.

2.2 History

The concept of the LHC was officially recognized during a workshop held by CERN and the European Committe for Future Accelerators (ECFA) during 21-27 March 1984. The tunnel that would later house the LHC, was constructed between 1983-1988 for the Large Electron-Positron Collider experiment.

The construction of the LHC was completed in 2008, and in September that year, the first beam of protons was steered around the LHC ring. After initial lower energy collision runs in 2009, the first 7 TeV center of mass energy collisions were recorded in 2010.

2.3 Design
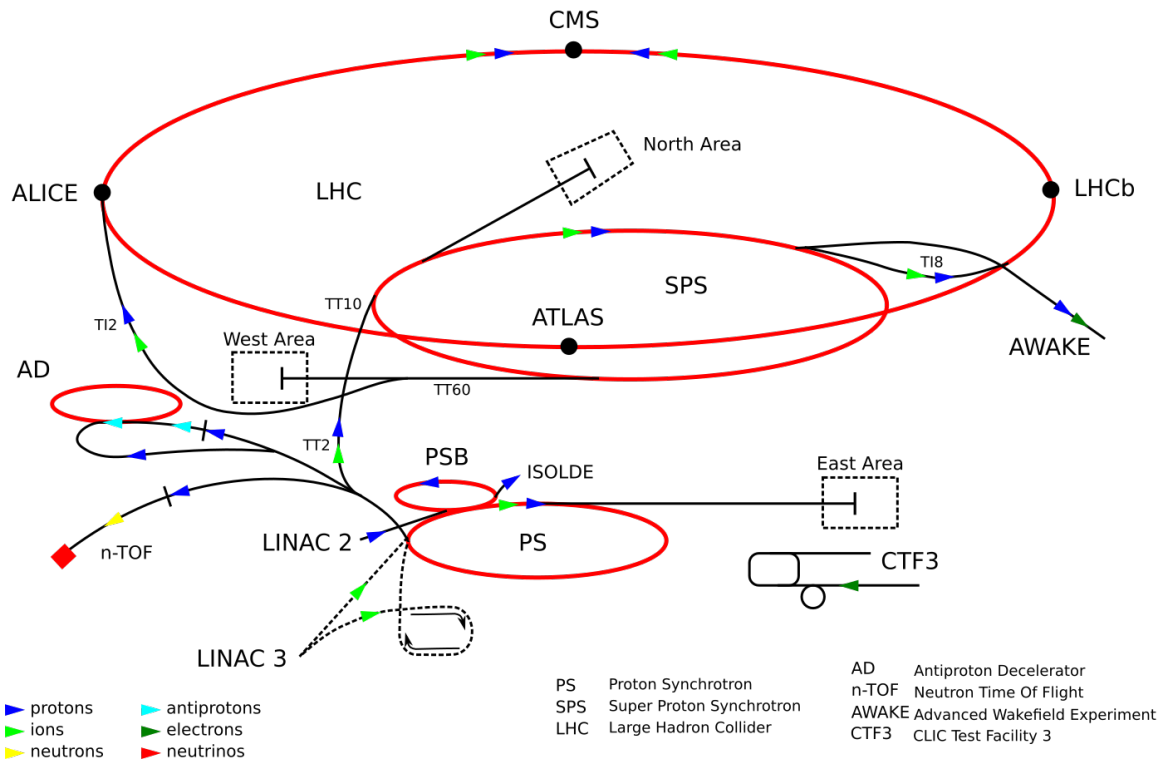
Figure 2.1: The CERN accelerator complex showing the various components of the Large Hadron Collider experiment, such as the linear accelerators, the accelerating synchrotrons, the main ring, and the four detectors, where the protons or heavy ions are collided.

The LHC is contained in a circular tunnel 26.7 km in circumference, located at a depth ranging between 50 and 175 meters underneath the border between Switzerland and France. The tunnel houses two parallel beam pipes. Each of the two beam pipes contain a beam of protons (or heavy ions), composed of several bunches of particles, which travel in opposite directions, until they are made to collide at 4 points where the beam pipes intersect. The beams are aligned and steered by an array of 1232 superconducting dipole magnets. An additional 392 superconducting quadrupole magnets focus the beams to maximize the chance of interaction. Magnets of higher mulitpole orders are used to correct deviations in the field geometry.

The colliding protons are prepared for collisions by a sequence of systems, such as LINAC 2 (a liner accelerator), the Proton Synchrotron Booster (PSB), the Proton Synchrotron (PS), and the Super Proton Synchrotron (SPS), which progressively increase their energy. The highly energetic protons (having an energy of about 450 GeV each) are then injected into the LHC ring.

Instead of a continuous beam, the protons are accumulated into bunches and accelerated to their peak energy at 6.5 TeV over a period of 20 minutes, and circulated for up to 24 hours while collisions occur at the four intersection points. Each proton bunch consists of approximate 1.15×10^{11} protons in each bunch, with 2,556 bunches [36] at a time. The interactions happen at intervals 25 nanoseconds apart. Figure 2.1 shows the layout of the LHC main ring, LINAC2, PSB, PS and SPS.
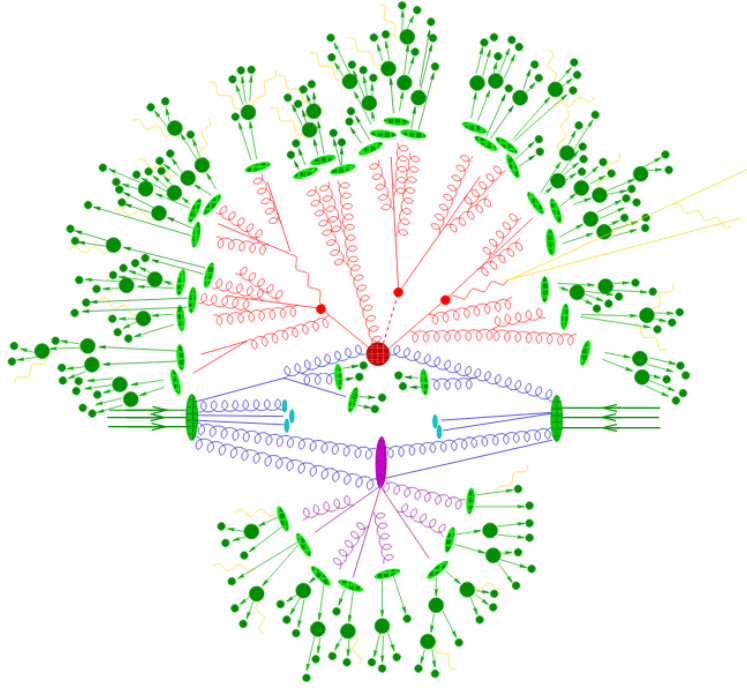
Figure 2.2: Overview of a proton-proton pp collision. The initial partons inside the protons (the green ovals) undergo initial state radiation, and interact in the hard process (red circle). The hard interaction results in a shower of partons (red curves) that hadronise into color neutral states (light green circles). The proton remnants then participate in a secondary interaction (purple ellipse) creating another parton shower (in purple), which hadronises and decays into stable particles. This, along with the beam remnants (light blue ellipses), is part of the underlying event. Charged particles can emit electromagnetic radiation (yellow) at any point.

2.4 Proton-Proton Collisions

Theory and experiment go hand in hand. It is necessary to have experimental confirmation of theoretical predictions, while at the same time, new or unexpected experimental observations prod theories along in the right direction. There are a number of parameters in theory that are unknown, and thus, experiments provide measurements of such parameters.

The work in thesis was conducted with the ATLAS Collaboration. ATLAS, being one of the detector experiments at the LHC, probes proton-proton collisions. Figure 2.2 shows a proton proton collision in detail. This section gives an overview of the physics of proton-proton collisions, which are one of several ways to probe particle interactions at high energy scales.

Protons are baryons, bound states of three quarks (*uud*), known as the valence quarks. However, the mass of the quarks put together is only about 1% of the mass of the proton (938 MeV). The remainder of the proton mass originates from the QCD binding energy, which is the exchange of virtual quarks and gluons. The constituents of the proton, namely the quarks and gluons, are collectively known as partons. Roughly half the total momentum of the proton is carried by the gluons [8]. Now, the number of gluons is not conserved, and they are capable of self interaction, the gluon structure within a proton is not constant. Gluons produce virtual $q\bar{q}$ pairs that again annihilate on timescales of the order $t_{virt} = 1/\Delta E$ [37]. A color-charged particle with sufficient energy to probe the particle structure of the proton is capable of interacting with a color-charged parton (quark or gluon). Interesting physics in pp collisions are initiated by qq, $q\bar{q}$, qg and gg scattering.

The fraction of proton momentum carried by a parton is not deterministic, because of the unpre-

dictable gluon structure. It is, however, possible to model the parton momenta as a probability distribution. For proton with momentum P, a parton of a given type carrying a momentum xP is given by the **Parton Distribution Function** (PDF) $f(x, Q^2)$, where x is the fraction of momentum carried by the parton, and Q is the momentum transfer of the interaction [37], and sets the scale at which the incoming particle is able to resolve the partons. QCD predicts quantitatively the rate of change of parton distributions when the energy scale Q^2 varies, governed by the DGLAP equations (names after the authors; Dokshitzer,Gribov,Lipatov,Altarelli,Parisi) [38], in the region where perturbative calculations can be applied. While the DGLAP differential equations give the energy scale Q^2 dependence, they cannot predict the x dependence of the parton distributions at a given Q^2. The PDFs sets must be obtained from fits on experimental data from $e^\pm p$ deep inelastic scattering (DIS), and hadron collider data. It is helpful to use electrons to probe protons structure as electrons don't have color charge. Fits are carried out on a large number of cross section data points, on a grid of Q^2 and x values from several experiments. This work is carried out by groups such as MSTW [39–41], MMHT [42], NNPDF [43], etc. Figure 2.3 shows an example of parton distribution functions.
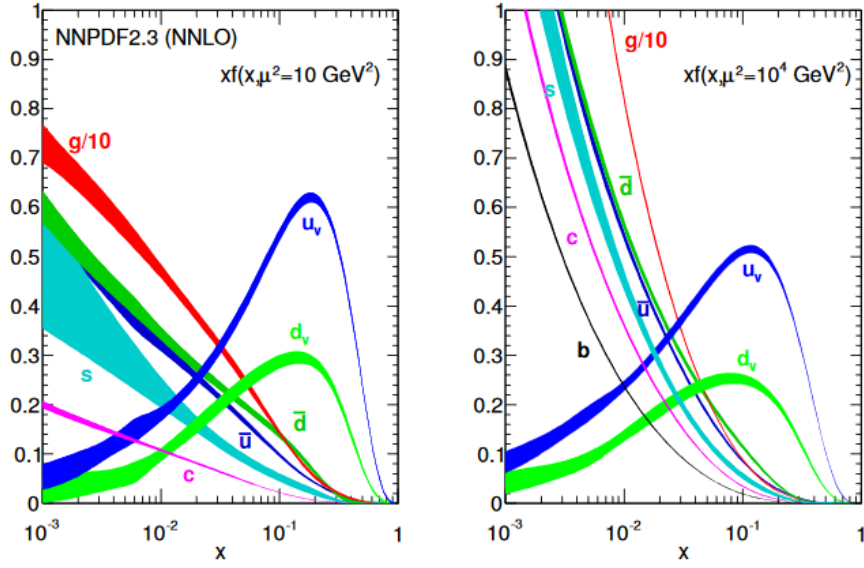
Figure 2.3: Parton Distribution Functions from NNPDF3.1, reproduced from [43]. The y-axis displays the probability of the given parton as a function of the proton momentum fraction, given on the x-axis. As seen here, the u quark has about 66% probability, and the d-quark has about 30% probability of possessing 10% of a protons momentum. Thus the proton's quark content is uud. Here, μ^2 is used in place of Q^2 to denote the momentum transfer.

The rate at which a scattering process occurs is called the cross section σ of the process. The cross section is expressed in barns, a unit of area, where $1b = 10^{-24} cm^2$. The number of collisions is characterised by the luminosity $\mathscr{L}$. The luminosity is indicative of the performance of a particle accelerator, and is defined as the ratio of the rate of event detection to the cross section (Equation 2.1):

$$\mathscr{L} = \frac{1}{\sigma}\frac{dN}{dt} \tag{2.1}$$

The rate of events having a final state X will then be given by Equation 2.2.

$$\frac{dN_X}{dt} = \sigma(pp \to X)\mathscr{L} \tag{2.2}$$

For head-on colliding protons, each with momentum P, such that their center-of-mass energy is $\sqrt{s} = 2P$, the interacting partons will have a total energy $\sqrt{\hat{s}} = \sqrt{2x_1x_2}P$, where x_1 and x_2 give the fraction of its proton momentum carried by each parton. For the process $pp \rightarrow X$, the cross section is calculated using Equation 2.3.

$$\sigma(pp \rightarrow X) = \sum_{n=0}^{\infty} \alpha_S^n(\mu_R^2) \sum_{i,j} \int dx_1 dx_2 f_{i/p}\left(x_1, \mu_F^2\right) f_{j/p}\left(x_2, \mu_F^2\right) \times \hat{\sigma}_{ij \rightarrow X}^{(n)}\left(x_1 x_2 s, \mu_R^2, \mu_F^2\right) \quad (2.3)$$

where $f_{i/p}$ and $f_{j/p}$ are the parton distrbution functions describing the fraction of proton momentum carried by the ith and j^{th} partons. Here, n is the order of α_S at which the cross section is calculated. If $X = ZZ$, such as for the process $pp \rightarrow ZZ$, at LO ($n = 0$) the hard (partonic) cross section $\hat{\sigma}_{ij \rightarrow ZZ}^{(n)}\left(x_1 x_2 s, \mu_R^2, \mu_F^2\right)$ is proportional to $\delta(x_1 x_2 s - M_Z^2)$. Thus, this term non zero only for partons i, j if they can produce a Z boson, such as $i = q$ and $j = \bar{q}$. For $n \geq 1$, partonic channels such as gq and gg also contribute, and there is no restriction for $x_1 x_2 s = M_Z^2$. Equation 2.3 also illustrates the dependence of the cross section on renormalization and factorization scales, μ_R and μ_F respectively. The separation of the calculation into perturbative hard scattering physics and non-perturbative Parton Distribution Functions greatly simplifies QCD calculations.

2.5   The ATLAS experiment

The ATLAS (A large ToroidaL ApparatuS) detector is located at one of the four beam intersection points. It is a multipurpose experiment which, after the discovery of the Higgs boson in 2012, focuses on a wide range of topics, including searches for new physics, such as supersymmetry or dark matter, and measurements of Standard Model parameters. The experiment is a collaboration between around 4000 physicists from over 175 institutions in 38 countries.

The ATLAS detector is a large apparatus with a cylindrical geometry, forward-backward symmetry, and nearly 4π solid angle coverage. It is 46 meters long, 25 meters in diameter and weight 7000 tonnes. The detectors consists of concentric cylindrical layers around the interaction point, where the proton beams collide. Broadly, it consists of the Inner Detector, the electromagnetic (EM) and hadronic calorimeters, the muon spectrometers and the magnetic systems, each composed of multiple layers. These layers complement each other's functionality: the inner detector accurately tracks charged particles passing through it, the calorimeters measure the energy deposited by the particles passing through or stopped by it, the magnet systems employ the Lorentz force law to bend charged particles and measure their momenta, and the muon systems measure the momenta of muons that pass through all other layers to reach it. Figure 2.4 displays the ATLAS detector and its components.

The Inner Detector (ID) is built to accurately track the trajectory and curvature of charged particles as they pass through it, to measure their momenta. The calorimeters measure the energy deposited in them by charged and neutral particles. Photons and electrons completely deposit their energy into the EM calorimeters, while hadrons, being heavier, pass through the EM calorimeter without losing much of their energy to deposit most of it into the hadronic calorimeters, which lie outside the EM calorimeters. The magnet systems are composed of large superconducting magnets that bend the paths of charge particles moving through their magnetic field, allowing the measurement of their momenta. Muon are stable particles that pass through all the inner layers of the detector and reach the outmost part, which is the Muon Spectrometer. The Muon Spectrometers accurately measures the path taken by muons, and their curvature, to measure their momenta, providing an important trigger to select events with high energy muons.

The ATLAS detector cannot detect neutrinos or other weakly interacting neutral particles; their existence is inferred from the momentum imbalance from the detected stable particles that register in
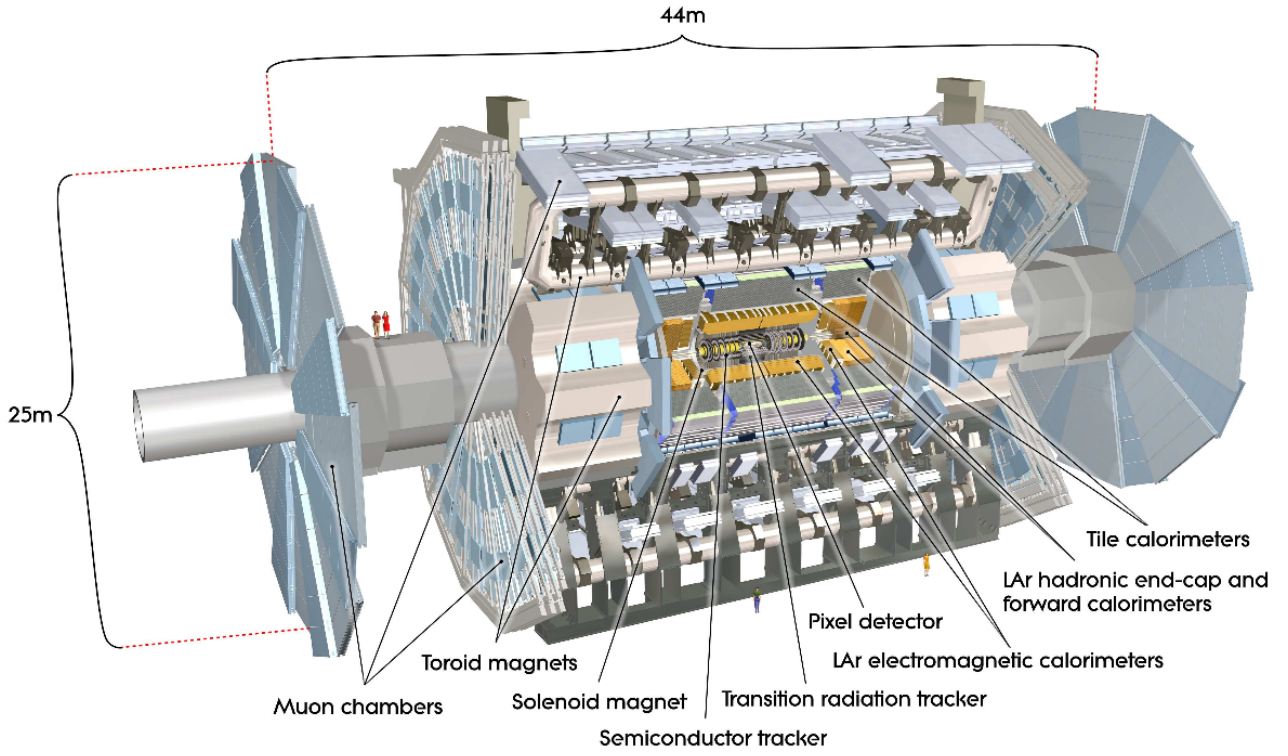
Figure 2.4: Illustration of the ATLAS detector, displaying its dimensions and components, reproduced from Ref [44]

the detector components. Thus, the detector must be "hermetic", and must have no blind spots. In proton-proton collisions, the interactions actually happen between quarks and gluons (partons) that make up the proton. These partons carry a fraction of the proton momentum, which is not deterministically known, but can be modelled using probability distribution functions. Thus applying momentum conservation along the beam axis is not possible. However, these partons have negligible or no momenutum in the transverse plane, and thus the momentum imbalance can be accurately calculated in the transverse plane, and is called missing transverse momentum, denoted by E_T^{miss} .

2.5.1 Coordinate system

ATLAS employs right-handed Cartesian coordinate system, with the origin defined as the interaction point. The direction of the beam defines the z-axis. The x-axis is defined such that it points towards the center of the LHC ring, while the y-axis is defined vertically. The xy-plane is taken as the transverse plane, described by the polar coordinates (r, ϕ) such that $\phi = 0$ on the x-axis. The pseudorapidity replaces the polar angle θ as given in Equation 2.4. Some values of the pseudorapidity are shown in Figure 2.5.

$$\eta = -ln\left(tan\left(\frac{\theta}{2}\right)\right) \tag{2.4}$$

In the limit where the mass of particles is much less than their momentum, it is approximately equal to the rapidity (y) of the particle. The rapidity,

$$y = \frac{1}{2}ln\left(\frac{E + p_z}{E - p_z}\right), \tag{2.5}$$
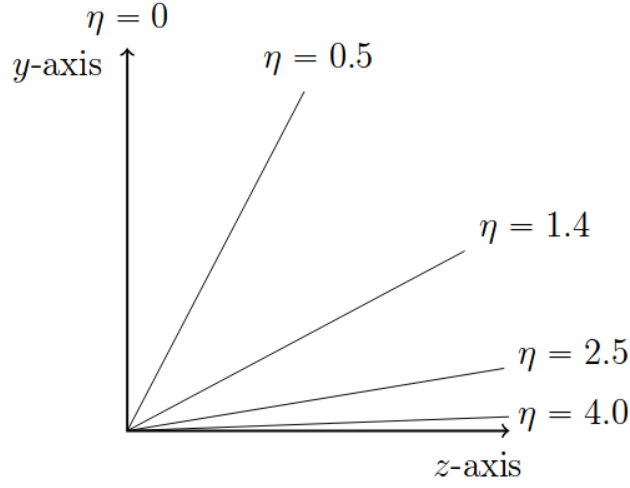
Figure 2.5: Some important and often mentioned values of pseudorapidity η.

in turn, is an effective coordinate due to its Lorentz invariance under boosts in the z-direction.

The separation between two objects in the detector is described by

$$\Delta R = \sqrt{\Delta \eta^2 + \Delta \phi^2} \tag{2.6}$$

where ϕ is the angular coordinate in the transverse plane.

2.6 Event Simulation

It is essential to have some reference to compare with when interpreting LHC data. The observations must be compared to expected outcomes predicted by physical models, such as the Standard Model or SUSY. Thus, ATLAS uses event simulation, beginning from the initial proton proton collitions, leading up to the process(es) of interest, up to the expected detector response.

Events in a given process are generated using Monte Carlo methods, where points in the kinematic phase-space are chosen using random sampling. These are used in Monte Carlo generator software such as MadGraph [50] to calculate the matrix element of the process. Such generators use parton distribution functions (PDFs) to model the interaction between partons up to a given order in QCD, with higher order corrections being accounted for by a "k-factor". The radiating partons after the hard interaction result in a shower, which are modelled by parton showering software, such as Pythia [51]. The output of these steps is input into the next step of simulation, and is also used for generator-level studies, called "truth-level".

In the next step, called detector simulation, the particles are propagated through the various layers of the detector, where the effects of the detector material, and it interaction with the particles, are accounted for in the simulation. The goal is to have a resulting data set identical to the one obtained from the physical detector. Software such as Geant4 [52]. This is a slow process, and often a faster but more approximate detector simulation is used. Detector simulation digitizes the interaction of particles by emulating the response of the electronics in the detector.

The data after the simulation of the detector is used to identify and reconstruct objects as particles, such as muons, electrons, photons or jets. Energy deposits that are not identified and matched to physical objects are collected together as "soft-terms" that are used to calculate the missing transverse energy E_T^{miss} .

19

2.6.1 Missing Transverse Momentum

Stable particles that do not interact electromagnetically or hadronically pass through the various detector layers without interacting, and are thus not visible to the detector. Collisions between the partons (which carry some fraction of the proton's momentum) take place along the beam axis (z-axis). Along the x- and y-axes, i.e. in the transverse place, the momentum before the collision in zero. Thus such invisible objects are identified by an imbalance in the total momentum in the transverse plane. Thus, the missing transverse momentum, defined as the negative vector sum of the transverse momenta of all visible reconstructed objects in the event,

$$\vec{p}_T^{\text{miss}} = - \sum_{visible} \vec{p}_T \tag{2.7}$$

where visible objects include muons, electrons, photons, taus, jets, and the soft-terms that do not correspond to physical objects.

For predicted particles with high mass, or particles that carry high momentum away from the hard interaction vertex, a large imbalance is expected.

The magnitude of the $\vec{p}_T^{\text{miss}}$ is denoted by E_T^{miss} .

Chapter 3

Analysis Strategy

3.1 Invisible Higgs in association with a Z boson - ZH

In the search for Dark Matter candidates, some Beyond Standard Model theories postulate that the Higgs boson mediates the interaction between Dark Matter particles and Standard Model particles, as shown in Figure 3.1. In this thesis, the production of the Higgs boson, in association with a Z boson is considered. The Higgs boson decays into Dark Matter candidates (Weakly Interacting Massive Particles, or WIMPS), and the Z boson decays into a charged lepton-antilepton pair. As Dark Matter is invisible to current detectors, this process results in the $\ell\ell + E_T^{\mathrm{miss}}$ signature.
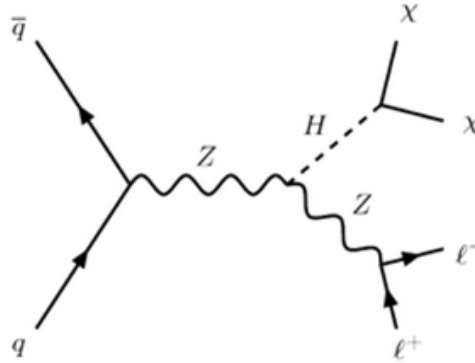
Figure 3.1: Feynman diagram showing the associated production of a Higgs boson with a Z boson. The Higgs boson decays to two invisible Dark Matter particles and the Z boson decays leptonically, resulting in the $\ell\ell + E_T^{miss}$ signature.

The main Standard Model background processes for the $\ell\ell + E_T^{\mathrm{miss}}$ final state are $ZZ \to \ell\ell\nu\nu$, $WZ \to \ell\ell\ell\nu$, $WW \to \ell\nu\ell\nu$, Z+jets and W+jets.

3.1.1 Selection Criteria

The selection criteria used in Ref [53] is applied for the analysis reported in this thesis as well. The search is conducted on events with a $\ell\ell + E_T^{\mathrm{miss}}$ final state, having a pair of high p_T electrons (ee) or muons ($\mu\mu$), and large missing transverse momentum. Events with extra leptons or b-jets are removed to reduce backgrounds, and the requirement of a boosted Z boson back to back with the missing tranverse momentum vector is imposed. Electron candidates are selected based on the

21

ATLAS tracker and EM calorimeter dimensions, with $p_T > 7$ GeV and pseudorapidity $|\eta| < 2.47$.
Similarly, muon candidates are required to have $p_T > 7$ GeV and pseudorapidity $|\eta| < 2.5$.

The leading and subleading leptons in the event are required to have sufficiently high transverse momentum, with the leading lepton required to have $p_T > 30$ GeV, and the subleading lepton required to have $p_T > 20$ GeV. The veto on additional leptons serves to remove background from processes such as $WZ \to \ell\ell\ell\nu$. The reconstructed mass of the leading and subleading leptons is required to be within a 15 GeV window around the mass of the Z boson, i.e. $76 < m_{\ell\ell} < 106$ GeV, to suppress backgrounds where the final state leptons do not originate from a Z boson (non-resonant $\ell\ell$ processes). As the leading and subleading leptons are expected to come from the decay of a highly boosted Z boson, their separation is expected to be small. Thus, the leading and subleading leptons in selected events are required to be separated by $\Delta R_{\ell\ell} < 1.8$. The E_T^{miss} is expected to be back to back to a Z boson with high p_T, and originates from an invisibly decaying Higgs boson, thus is expected to be high as well; a cut requiring $E_T^{\mathrm{miss}} > 90$ GeV reduces the number of events with low E_T^{miss}. The requirement of back to back Z boson and E_T^{miss} is enforced by requiring the angular separation of the E_T^{miss} vector from the Z boson candidate vector in the transverse plane, $\Delta\phi(\vec{p_T}^{\ell\ell}, \vec{E}_T^{miss})$ to be greater than 2.7 radians. Z+jets background events have large E_T^{miss} because of significant contribution from soft terms. To remove this background, the magnitude of the difference between the dilepton transverse momentum $p_T(\ell\ell)$ and the sum of the jet p_T and E_T^{miss} must be less than 20% of the dilepton p_T. To suppress $t\bar{t}$ and Wt backgrounds, events with one or more b-jets (jets that originate from a b-quark, such as from the decay of a top quark) are vetoed.

Table 3.1 summarises the event selection criteria in the $\ell\ell + E_T^{\mathrm{miss}}$ search, as shown in [53].

	Selection criteria
Two leptons	Two opposite-sign leptons, leading (subleading) $p_T > 30$ (20) GeV
Third lepton veto	Veto events if any additional lepton with $p_T > 7$ GeV
$m_{\ell\ell}$	$76 < m_{\ell\ell} < 106$ GeV
E_T^{miss} and E_T^{miss}/H_T	$E_T^{\mathrm{miss}} > 90$ GeV and $E_T^{\mathrm{miss}}/H_T > 0.6$
$\Delta\phi(\vec{p}_T^{\ell\ell}, \vec{p}_T^{miss})$	$\Delta\phi(\vec{p}_T^{\ell\ell}, \vec{p}_T^{miss}) > 2.7$ radians
$\Delta R_{\ell\ell}$	$\Delta R_{\ell\ell} < 1.8$
Fractional p_T difference	$\left| p_T^{\ell\ell} - p_T^{miss,jets} \right| / p_T^{\ell\ell} < 0.2$
b-jet veto	$N(b\text{-jets}) = 0$ with b-jet $p_T > 20$ GeV and $|\eta| < 2.5$

Table 3.1: Event selection criteria in the $\ell\ell + E_T^{\mathrm{miss}}$ search as shown in ATLAS ZH search [53]

3.1.2 Results of the ZH search

Using the selections in Table 3.1, background predictions are made in the $\ell\ell + E_T^{\mathrm{miss}}$ channel. Figure 3.2 shows the observed E_T^{miss} distribution in the ee and $\mu\mu$ channels, compared to the signal and background predictions. As discussed in Ref [53], the dominant source of background is the $ZZ \to \ell\ell\nu\nu$ process, contributing $\approx 60\%$ of the background. $WZ \to lll\nu$ events, where the W boson decays into a electron or muon that escapes detection, account for 25% of the total background. $Z(\to ll)$+jets process with misreconstructed E_T^{miss} contributes to about 8% of the total background, and non-resonant-ll processes, consisting of $t\bar{t}$, Wt, WW and $Z \to \tau\tau$ production contribute similarly. W+jets, VVV, and $t\bar{t}V(V)$ backgrounds contribute to a minor extent ($< 1\%$).

An upper limit of 67% is placed on the Higgs→ Dark Matter branching ratio at the 95% confidence level.
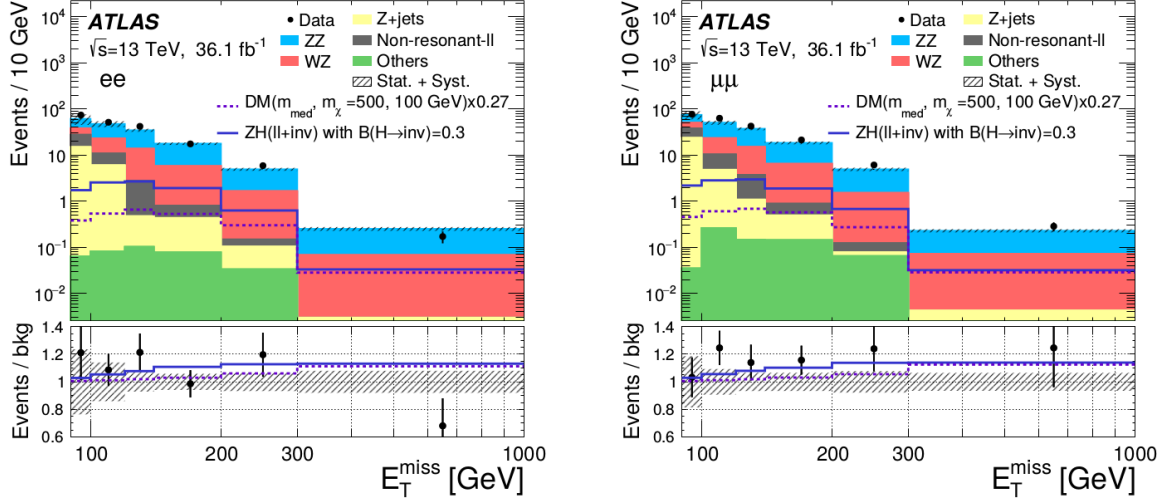
Figure 3.2: The observed E_T^{miss} distributions in the *ee* (left) and $\mu\mu$ channels, compared to the signal and background predictions, reproduced from Ref [53]. The total statistical and systematic uncertainty on the background predictions are shown by the error bands. The Standard Model background predictions are stacked. The $ZH \to ll+$ invisible signal distribution is shown with $B_{H \to inv} = 0.3$. The dotted line shows an alternative model for Dark Matter production that is not discussed in this work.

This thesis focuses on improving the *ZZ* background background estimate. In Ref [53], the *ZZ* background is estimated from simulation with a total uncertainty of 10%.

3.2 Background estimation: ZZ

It is difficult to distinguish the irreducible $ZZ \to \ell\ell\nu\nu$ background events from the signal process, as the final state is experimentally indistinguishable from to that of $ZH \to \ell\ell + E_T^{\mathrm{miss}}$. The contribution of $ZZ \to \ell\ell\nu\nu$ is currently estimated using simulation. Figure 3.3 shows the Standard Model production of $q\bar{q} \to ZZ$ and $gg \to ZZ$. One of the Z bosons decays leptonically (into e^+e^- or $\mu^+\mu^-$), while the other Z boson decays into neutrinos ($\nu\bar{\nu}$). Neutrinos are very weakly interacting, and thus are invisible to the detectors at the LHC, and thus result in events with missing transverse momentum.
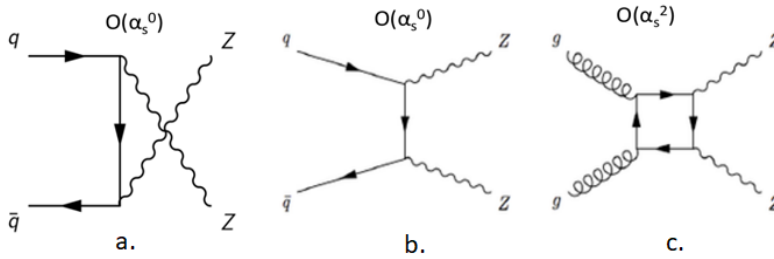
Figure 3.3: Feynman diagram showing *ZZ* production, in the s-channel (a) and t-channel (b) induced by $q\bar{q}$ at LO QCD, and induced by gluons (c) at NNLO QCD.

It is possible to estimate the $ZZ \to \ell\ell\nu\nu$ using $ZZ \to \ell\ell\ell\ell$ data. However, the precision of this method would be severely limited by the small number of $ZZ \to \ell\ell\ell\ell$ events in data. The branching fraction

$Z \to \ell\ell$ for one flavor of lepton (e/μ) is $\approx 3.4\%$, and $Z \to \nu\nu$ is 20%.

$$BR(ZZ \to \ell\ell\ell\ell) = (2 \times 0.034) \times (2 * 0.034) = 0.00462 \tag{3.1}$$
$$BR(ZZ \to \ell\ell\nu\nu) = (2 \times 0.034) \times (0.2) \times 2 = 0.0272 \tag{3.2}$$

Thus, branching fraction of $ZZ \to \ell\ell\ell\ell (\approx 0.46\%)$ compared to $ZZ \to \ell\ell\nu\nu$ (2.7%) is smaller by a factor of 6. The low branching fraction of $ZZ \to \ell\ell\ell\ell$ limits the precision. The statistics are further limited by detector effects.

Motivated by an analysis using γ+jets to estimate Z+jets [54], an alternative method to estimate $ZZ \to \ell\ell\nu\nu$ is to look at the $Z\gamma \to \ell\ell\gamma$ process. Figure 3.4 shows the leading order diagrams for the production of $Z\gamma$, where the Z boson further decays leptonically. Figures 3.4.a, b and c are similar to the production of ZZ, with a photon instead of one of the Z bosons. The main differences in the two processes are the couplings of the photon and Z boson to the quarks, and the fact that photons are massless, whereas the Z boson is massive.

Figure 3.4.d shows the Final State Radiation (FSR) diagram for the $\ell\ell\gamma$ final state. The photon is in this case radiated off a final state lepton. This process must be suppressed as it does not correspond to a similar $ZZ \to \ell\ell\nu\nu$ process. Imposing a mass window requirement on the reconstructed Z boson candidate mass suppresses this diagram.
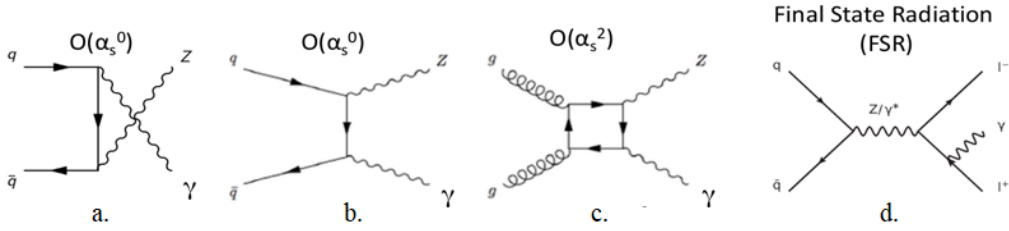
Figure 3.4: Feynman diagram showing $Z\gamma$ production, in the s-channel (a) and t-channel (b) induced by $q\bar{q}$ at LO QCD, and induced by gluons (c) at NNLO QCD. Diagram (d) shows a similar final state, but the photon is radiated off of a final state lepton (Final State Radiation), which does not have a corresponding diagram in the $ZZ \to \ell\ell\nu\nu$ process, and hence has to be suppressed.

At high Z boson transverse momentum, the $Z\gamma \to \ell\ell\gamma$ process should be similar to $ZZ \to \ell\ell\nu\nu$, as the mass of the Z boson will be negligibly small compared to its p_T. The $Z\gamma \to \ell\ell\gamma$ signal is also pure, and has a BR$\times\sigma$ as compared to $ZZ \to \ell\ell\nu\nu$. Thus, it should be possible to use $Z\gamma \to \ell\ell\gamma$ data to estimate the contribution of $ZZ \to \ell\ell\nu\nu$ in regions of high Z boson p_T.

3.3 Approach

This thesis plans to estimate the ZZ background contribution to the $ll+E_T^{\mathrm{miss}}$ final state using $Z(\to ll)\gamma$ data, where the photon models the Standard Model invisible Z boson. A transfer factor R is introduced as the ratio of the cross sections of $ZZ \to \ell\ell\nu\nu$ to $Z\gamma \to \ell\ell\gamma$. In the high Z boson p_T region, the two processes are kinematically similar, therefore the curve of the transfer factor R as a function of p_T is expected to approach a constant value. This transfer can be used to estimate to the contribution of $ZZ \to \ell\ell\nu\nu$ from $Z\gamma \to \ell\ell\gamma$ data.

A ratio of the cross sections of $ZZ \to \ell\ell\nu\nu$ and $Z\gamma \to \ell\ell\gamma$ processes is taken to obtain the R distribution as a function of E_T^{miss}, or $p_T(\gamma)$. The uncertainty on R is calculated by estimating the possible effect

24

588 of missing higher order corrections, the PDF sets used, photon fragmentation, etc. The contributions
589 of the $q\bar{q}$ and gg processes are estimated separately.

3.4 Transfer factor R

591 To estimate the background, a transfer factor $R(p_T)$ is introduced, defined to be the ratio of the cross
592 sections of $ZZ \to \ell\ell\nu\nu$ to $Z\gamma \to \ell\ell\gamma$ as a function of the p_T.

$$R(p_T) = \frac{\sigma_{ZZ}(p_T)}{\sigma_{Z\gamma}(p_T)} \tag{3.3}$$

593

594 With the two processes being kinematically similar at high p_T, R depends on the coupling of the Z
595 and γ to quarks. It would be expected to reach a constant value at high p_T that can be determined the-
596 oretically. In the following paragraph, an attempt is made to obtain a simple approximate calculation
597 of R from the contribution of qq process.

598 The photon - quark and Z boson - quark couplings in the Standard Model are given by,

$$-ieQ_q\gamma^{\mu} \qquad \text{and} \qquad \frac{-ie}{2\sin\theta_W\cos\theta_W}\gamma^{\mu}(v_q - a_q\gamma_5) \tag{3.4}$$

599

600 respectively, where Q_q, v_q and a_q are respectively the electric, vector and axial neutral weak cou-
601 plings of the quarks, and θ_W is the weak mixing angle. There is a contribution due to the Z mass
602 which appears in the internal propagators and phase space integration. This contribution becomes
603 less important in the $p_T(\gamma) \gg M_Z$ region.

604 Thus, the leading order contributions from $q\bar{q} \to ZZ$ and $q\bar{q} \to Z\gamma$ are shown in Equation 3.5.

$$\sigma(q\bar{q} \to ZZ) \propto \frac{1}{2}\frac{e^4\{(v_q^2 + a_q^2)^2 + 4v_q^2a_q^2\}}{16\sin^4\theta_W\cos^4\theta_W}$$

$$\sigma(q\bar{q} \to Z\gamma) \propto \frac{e^2Q_q^2(v_q^2 + a_q^2)}{4\sin^2\theta_W\cos\theta_W} \tag{3.5}$$

605

606 The u and d quarks present in a pp collision have different coupling strengths to the Z boson as stated
607 in Ref [55], their relative contributions are accounted for using Equation 3.6

$$R = \frac{\sigma(u\bar{u} \to ZZ)\langle u\rangle + \sigma(d\bar{d} \to ZZ)\langle d\rangle}{\sigma(u\bar{u} \to Z\gamma)\langle u\rangle + \sigma(d\bar{d} \to Z\gamma)\langle d\rangle} \tag{3.6}$$

608

609 Using the vector and axial couplings of the Z boson to u and d quarks[1], assuming $\langle d\rangle/\langle u\rangle = 0.5$ and
610 setting $\sin^2\theta_W = 0.2315$, $R \approx 1.28$ for the dominant $q\bar{q}$ interaction. This approximate calculation has
611 not been performed for gluon induced channels, as they involve loops and require a more involved
612 calculation. It will also give a significantly different value as the contributions of the gluon induced
613 channels are different for the ZZ and $Z\gamma$ processes.

614 This transfer factor R may be used with $Z\gamma$ data to estimate the contribution of ZZ with reasonable
615 accuracy at high p_T. To improve precision, it is necessary to estimate the theoretical uncertainties on
616 the transfer factor R.

---

[1] Vector and Axial couplings of Z to u and d quarks: $v_u = 0.18, a_u = 0.50, v_d = -0.35, a_d = -0.514$

3.5 Theoretical Uncertainties

In this study, the following sources of theoretical uncertainties are studied.

- Missing higher order corrections: Contributions due to higher order QCD corrections cannot be calculated to arbitrarily high order, as it gets progressively more computationally expensive. Thus, this study is limited to next to leading order (NLO), and further corrections are accounted for by varying the factorization and renormalization scales. The next section 3.6 discusses the approach taken to evaluate uncertainties associated with missing higher order corrections.

- Uncertainties associated with Parton Distribution Functions: According to the Parton model [56], a proton is composed of three valence quarks, and several gluons and virtual quarks. These quarks and gluons are called 'partons'. Proton-proton collisions, such as in the experiments conducted at the LHC, involve the interaction of these quarks and gluons at very high energies. These partons carry a fraction of the proton momentum. Parton Distribution Functions (PDFs) represent this fraction of proton momentum carried by partons as probability distributions. Owing to the non-deterministic nature of this fact, this study attempts to account for these uncertainties as PDF uncertainties.

- Photon Fragmentation Uncertainties: In the $Z\gamma \to \ell\ell\gamma$ process, the signal includes a photon. However, while reconstructing the event, soft photons, or photons resulting from other fragmentation processes may be encountered. To ensure that the photon is indeed prompt, it is required to be isolated from partonic activity. This isolation is implemented experimentally in different ways. The uncertainty associated with the modelling of photon fragmentation is estimated.

3.6 Renormalization

In Feynman diagrams beyond tree level, the introduction of self interaction loops, such as in Figure 3.5, lead to divergent integrals that are progressively more difficult to calculate at higher orders. A perfect calculation, carried out up to infinite orders, would give the exact cross section. However current technological capabilities limit the order to which calculations can be carried out.

Figure 3.5: Loop corrections to the propagator and vertex illustrated using a Feynman diagram showing $\gamma \to e^+e^-$, for example. These loops represent interactions that happen at very small distance scales (and corresponding, very high energy scales), and are calculated perturbatively in QCD.

While calculating loop corrections, two kinds of divergences are encountered: infrared divergences, and ultraviolet divergences. Infrared divergences occur when the integral diverges due to the contributions of particles with very low energies (or equivalently, interactions at large distances), and

typically involve terms featuring $1/k$, thus diverging as $k \to 0$. Ultraviolet divergences are logarithmic divergences involving the term $\int \mathrm{d}^4 k\ 1/k^4$. Integrals of this form simplify as terms involving $\int \ln(k)\mathrm{d}k$ that diverge as the integration variable approaches ∞, occurring at very high energy scales, or equivalently, interactions at extremely short distances. They correspond to physics at long and short distances. Here, long distances are those where soft interactions take place, away from the hard parton-parton interaction. Short distances are those where the hard parton parton interactions occur.

Thus, it is necessary to regularize such integrals, i.e. render the divergences finite, or have them cancel out somehow. Dimensional regularization is one such method of regularization, where the power of the momentum integration is shifted by an infinitesimally small amount 2ε, i.e. $\int \mathrm{d}^4 q/(2\pi)^4 q... \to \mu^{2\varepsilon} \int \mathrm{d}^{4-2\varepsilon} q/(2\pi)^4 q...$ A prefactor $\mu^{2\varepsilon}$ is introduced, where μ is an arbitrary scale, to ensure that all observables have the dimension of mass. Thus, regularization envelops the effect of these divergences into the arbitrary scale μ. Upon renormalizing these regularized integrals, the $1/\varepsilon$ divergent terms cancel out, leaving only the scale μ to be addressed. In QCD calculations, this scale appears as part of a scale dependent parameter, namely the running strong coupling constant ($\alpha_s(\mu)$). However, this scale μ is arbitrary. It does not represent a physical quantity at all, and is a tool to get the divergent integrals to behave.

The infrared divergences are addressed by the inclusion of the factorization scale μ_F, while the ultraviolet divergences are addressed by the inclusion of the renormalization scale μ_R. These parameters are arbitrary, and are set by hand. These are then varied between $\frac{1}{2}\mu < \mu < 2\mu$ to obtain an indication of the dependence of the matrix element on the scales.

A perfect calculation would include an infinite number of terms in α_S, and would result in the μ-dependent terms cancelling out perfectly, resulting in an answer that is independent of the choice of μ. However, perturbative QCD calculations get progressively more computationally expensive as the order of the perturbative theory increases. Thus, perturbative QCD calculations are only carried out up to a fixed order. In the absence of a perfect infinite order calculation, the variation of the factorization and renormalization scales gives an estimate of missing higher order contributions.

Varying the scales is not a complete treatment of the higher order QCD effects. In addition to it, the process dependent part of the missing higher order contributions will be treated using K-factors. These K-factors account for the corrections between the leading order and higher order calculations, and the difference between the K-factors of the two process will give a handle on the degree of correlation between the two processes.

3.7 Photon Isolation

The $Z\gamma \to \ell\ell\gamma$ process may contain photons that arise from the hadron showers. Photons that are produced in the hard interaction are well isolated from activity. However, photons may also be produced from the fragmentation of partons as part of a hadronic jet. A clean sample of well isolated photons is important to obtain efficient background rejection, and in this case, to obtain a clear picture of $Z\gamma \to \ell\ell\gamma$ events.

Experimentally, photon isolation is implemented with the following selection:

$$\sum_{\in R_0} E_T(\mathrm{had}) < \varepsilon_h p_T^\gamma \tag{3.7}$$

limiting the transverse hadronic energy $E_T(had)$ in a cone of size $R_0 = \sqrt{\Delta\eta^2 + \Delta\phi^2}$ around the photon, to some fraction of the photon p_T. This rejects events where the photon is associated with any hadronic activity in the cone. While this method works well for prompt photons, for non-perturbative

fragmentation, this method of isolation constrains the phase space of events with soft gluons, which hinders the cancellation of infrared divergences. This method is currently used in experimental analyses at ATLAS.

The smooth cone isolation method of Frixione [58] is an alternative isolation procedure, which simplifies calculations by avoiding photon-to-hadron fragmentation contributions, treats both gluons and quarks in the same way, and can be applied to experimental data in hadron-hadron, photon-hadron and electron-positron collisions. In the Frixione method, the following isolation prescription is applied to the photon:

$$\sum_{R_{j\gamma} \in R_0} E_T(\text{had}) < \varepsilon_h p_T^\gamma \left(\frac{1 - \cos R_{j\gamma}}{1 - \cos R_0} \right)^n. \tag{3.8}$$

where $R_{j\gamma}$ is the separation of the photon and the jth parton. This constrains the total hadronic energy inside a cone of radius $R_{j\gamma}$, for all separations $R_{j\gamma}$ less than a chosen cone size R_0. For $n = 0$, Equation 3.8 is equal to Equation 3.7, but for $n \geq 1$, this prescription allows soft radiation inside the photon cone and collinear singularities are removed. The inclusion of soft radiation makes the Frixione isolation infrared finite at all orders, can be applied to events having non-perturbative photon fragmentation, and avoids collinear singularities, that occur when a parton is collinear with the photon, by requiring it to be soft.

Chapter 4

Transfer factor R and the uncertainties associated with it

4.1 MCFM

Monte Carlo for FeMtobarn processes (MCFM) is a program that calculates cross sections for femtobarn-level processes at leading order(LO) or next to leading order (NLO) in QCD. NNLO predictions in QCD, and NLO electroweak corrections are also provided for some processes. In this study, MCFM v8.0 [59–62] is used to generate cross sections of $ZZ \to \ell\ell\nu\nu$ and $Z\gamma \to \ell\ell\gamma$ processes at NLO, with a selection of generator level cuts. The generation parameters in MCFM allow fine control over the sample, such as PDF sets, photon isolation, lepton and photon p_T and η, renormalization and factorization scales, etc. The samples are generated with cuts on $E_T^{miss} = p_T(Z \to \nu\nu)$ for the ZZ process and $p_T(\gamma)$ for the $Z + \gamma$ process. Table 4.1 lists the generator level settings used for the ZZ and $Z + \gamma$ processes. All lepton cuts are consistent with the ones used in the ATLAS $Z+E_T^{miss}$ analysis [53], as shown in Table 3.1.

Cuts	
M_{ee}	$76 < M_{ee} < 106$ GeV
Order	NLO
PDF set	PDF4LHC15_nlo
$p_T^{\text{lead}}(e)$	> 30 GeV
$|\eta^{lead}(e)|$	< 2.47
$p_T^{\text{sublead}}(e)$	> 20 GeV
$|\eta^{sublead}(e)|$	< 2.47
$p_T(V)$	> 90 GeV
Renormalization scale μ_R	$H_T = \sum_i p_{T,i}$
Factorization scale μ_F	$H_T = \sum_i p_{T,i}$

Table 4.1: Settings in input.DAT for MCFM. These parameters are common between the $ZZ \to \ell\ell\nu\nu$ (process 82) and $Z\gamma \to \ell\ell\gamma$ (process 300) processes. Here, V is a vector boson: $Z(\to \nu\nu)$ for the ZZ process and γ for the $Z\gamma$ process.

The constraint on M_{ee} in the case of $Z + \gamma$ suppresses backgrounds from non resonant $\ell\ell$ processes by ensuring that the lepton pair is from a Z boson decay only. Additionally, photon isolation is implemented using the Frixione [58] method, with $R_0 = 0.4$, $\varepsilon = 0.075$ and $n = 1$.

In MCFM generated events, leptonically decaying Z boson are constrained to an electron-positron pair only, i.e. $Z \to ee$. As electrons and muons have similar properties with the exception of mass, simply the branching fraction of $Z \to ee$ must be accounted for to obtain the inclusive value of R.

$$R_{inc} = R * \frac{BR(Z \to ee)}{BR(Z \to ee) * BR(Z \to \nu\nu) * 2} \tag{4.1}$$

4.2 Results

Using the settings listed in Table 4.1, the cross sections for $ZZ \to ee\nu\nu$ and $Z\gamma \to ee\gamma$ are generated at LO and NLO, shown in Figure 4.1. Throughout this analysis, these samples are used as the reference from which the transfer factor R is constructed, and provide the central value around which the uncertainties are calculated.
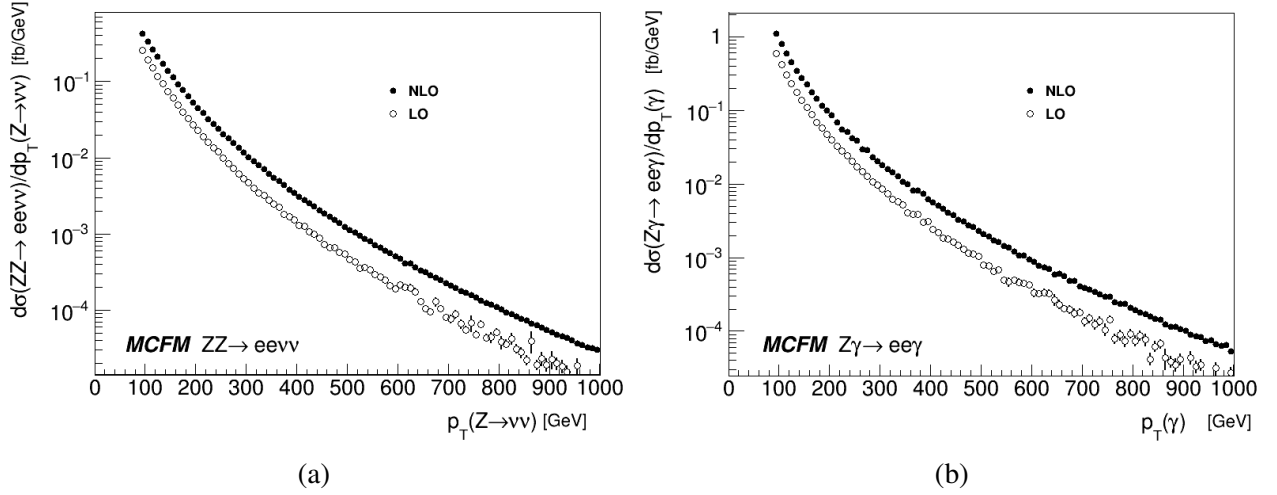
Figure 4.1: NLO and LO cross sections of $ZZ \to ee\nu\nu$ (left) and $Z\gamma \to ee\gamma$ (right) processes with the cuts as in Table 1. The leptonically decaying Z boson decays to an e^+e^- pair. The behaviour of the ratio of the NLO cross sections to the LO cross sections can be seen in Figure 4.9. There is no flavor constraint on the neutrinos.

There is a significant difference between the NLO cross section and LO cross section in both of these processes. The difference is greater at high p_T than at low p_T. However, the ratio of NLO to LO is similar between the two processes. Thus, the behavior of the transfer factor R at LO and NLO is expected to be similar at high p_T as well. This behavior is shown in Figure 4.9. The ratio $R = \sigma(ZZ \to ee\nu\nu)/\sigma(Z\gamma \to ee\gamma)$ at LO and NLO is shown in Figure 4.2a, taken as the ratio of the cross sections in Figures 4.1a and 4.1b.

The main differences between the ZZ and $Z\gamma$ processes are that the Z boson has a mass of 91 GeV, while the photon is massless, along with the different couplings of the Z boson and the photon to the different quark flavors. The difference in the masses of the bosons are expected to result in significant differences in the overall cross sections as well the kinematic behavior of the two processes. The PDFs are also sampled at different values of the parton momentum fraction x and momentum transfer Q^2 for the two processes.

30

In the regime where the mass of the Z boson is small when compared to the p_T of the Z boson and can be neglected, the x and Q^2 values become similar, and the kinematic behavior is expected to be more similar in this region. In that case the main difference remaining between the two processes are the different couplings of quarks to photons and Z bosons.
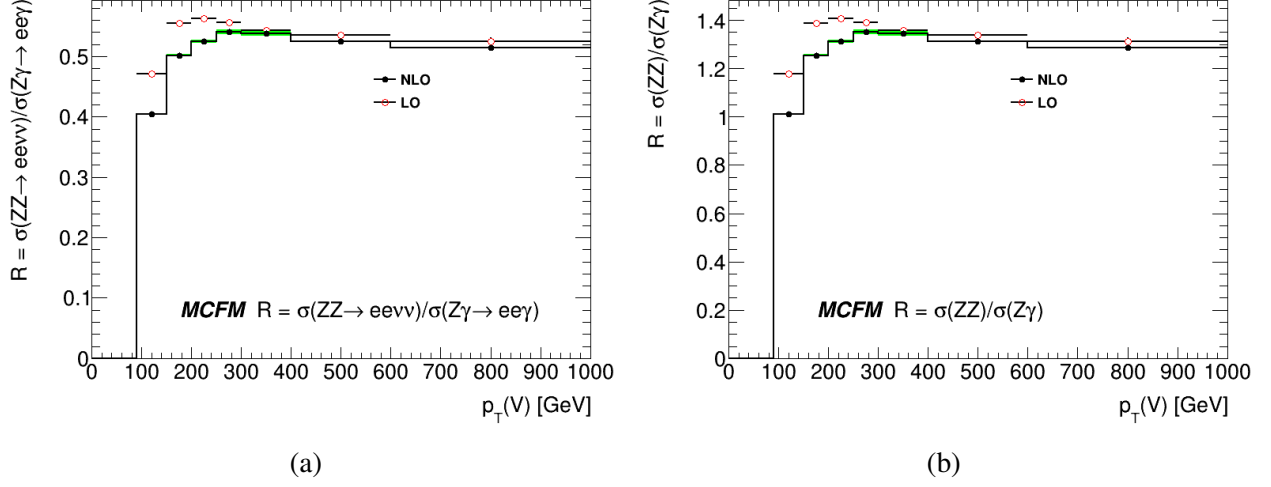
Figure 4.2: The transfer factor R as a function of p_T, taken as a ratio of the $ZZ \to ee\nu\nu$ and $Z\gamma \to ee\gamma$ cross sections at both LO and NLO. The figure on the left shows R calculated from cross sections as given by MCFM, where the the leptonically decaying Z boson decays into an e^+e^- pair. The figure on the right adjusts for the branching fractions of $Z \to ee$ and $Z \to \nu\nu$, thus showing $R = \sigma(ZZ)/\sigma(Z\gamma)$, where the Z bosons do not decay.

At NLO, the R value is observed to increase from ≈ 0.4 at 100 GeV to ≈ 0.52 at high p_T, where it reaches a plateau. At LO, the R value is about 20% larger at the lowest p_T values but at high p_T it is similar to the NLO R value. When the branching ratio of Z boson decaying selectively to e^+e^-, or to $\nu\nu$, is accounted for as shown in Equation 4.1, the resulting ratio $R(p_T)$ is shown in Figure 4.2b. Here, the ratio of $\sigma(ZZ)$ to $\sigma(Z\gamma)$ is shown, i.e. the Z bosons do not decay. The value of R is observed to increase from ≈ 1.08 at 100 GeV to ≈ 1.3 at high p_T. This agrees with the simple approximate calculation presented in Section 3.4 of $R \approx 1.28$.

Figures 4.3 and 4.4 further illustrate the topology of the events by showing normalized distributions for the leading and subleading lepton p_T and rapidity.
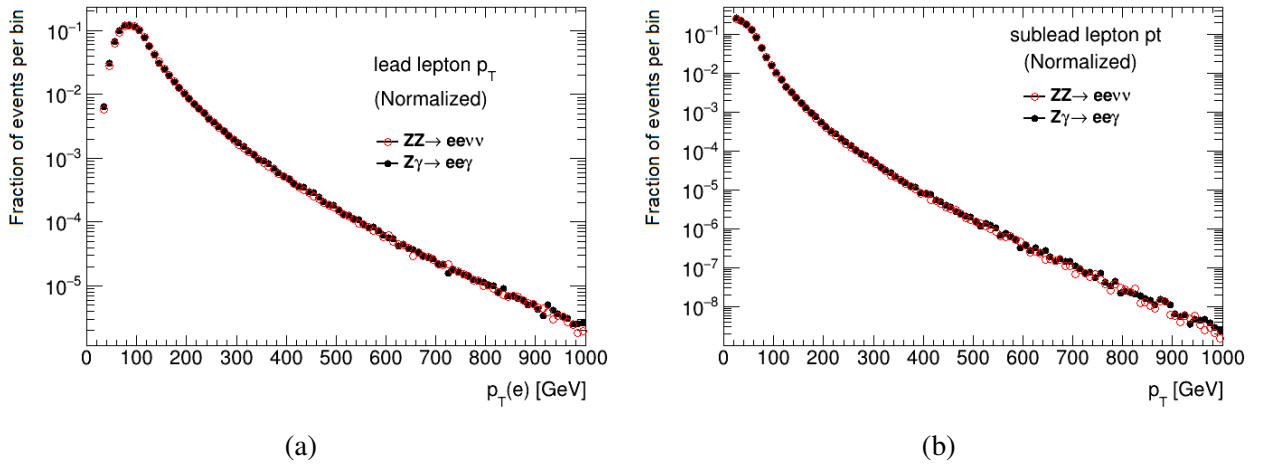
Figure 4.3: Normalized distributions showing the differential cross section as a function of the transverse momentum of the leading (left) and subleading (right) leptons for the two processes.

31

(a)   (b)
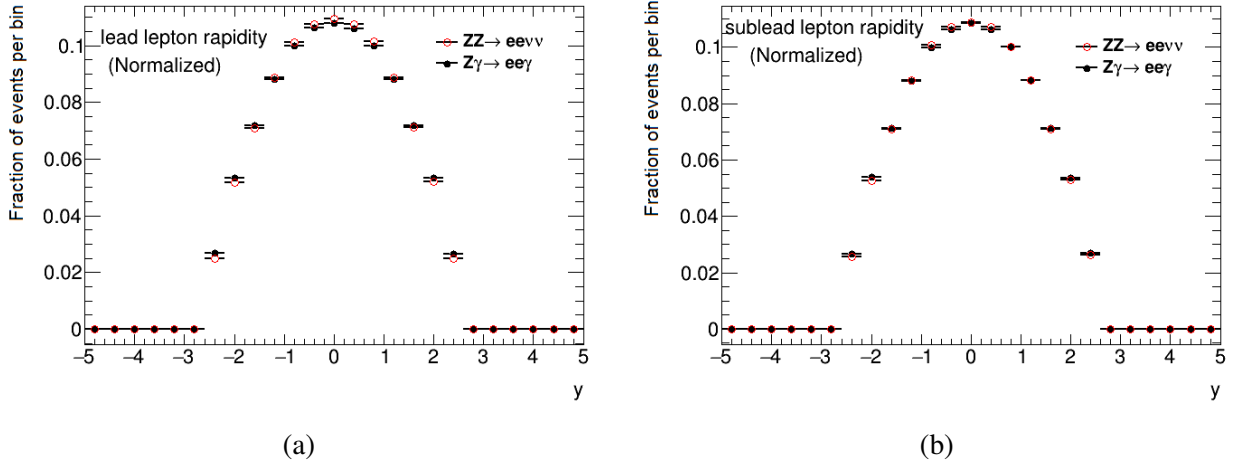
Figure 4.4: Normalized distributions showing the differential cross section as a function of the rapidity of the leading (left) and subleading (right) leptons1 for the two processes.

Figures 4.3 and 4.4 show that the leptons from a Z boson decay have very similar kinematic behavior between the two processes.

Gluon-gluon processes contribute to 8.6% of the total cross section for the ZZ process and 2.5% of the $Z + \gamma$ process. Figure 4.5 shows the $qg + q\bar{q}$ and gg contributions to the ZZ and $Z\gamma$ cross section. Interactions between partons carrying a low momentum fraction x result in low p_T final state particle. As seen in Figure 2.3, at low x, parton-parton interactions are dominated by gluons. The parton momentum fraction is given by

$$x = \frac{E_T(Z) + E_T(V)}{\sqrt{s}}$$

where $E_T = \sqrt{M^2 + p_T^2}$ for each final state particle. For $\sqrt{s} = 13$ TeV, at $p_T = 0$ GeV, $x \approx 0.007$ for $Z\gamma$, and $x \approx 0.014$ for ZZ. At $p_T = 500$ GeV, the mass of the Z boson becomes negligible in comparison with the p_T, thus $x \approx 0.08$ for both processes. From Figure 2.3, it is seen that the gluon distribution is a factor 3 higher at $x = 0.01$ than at $x = 0.1$. Thus gluon induced channels contribute more at low p_T than at high p_T.
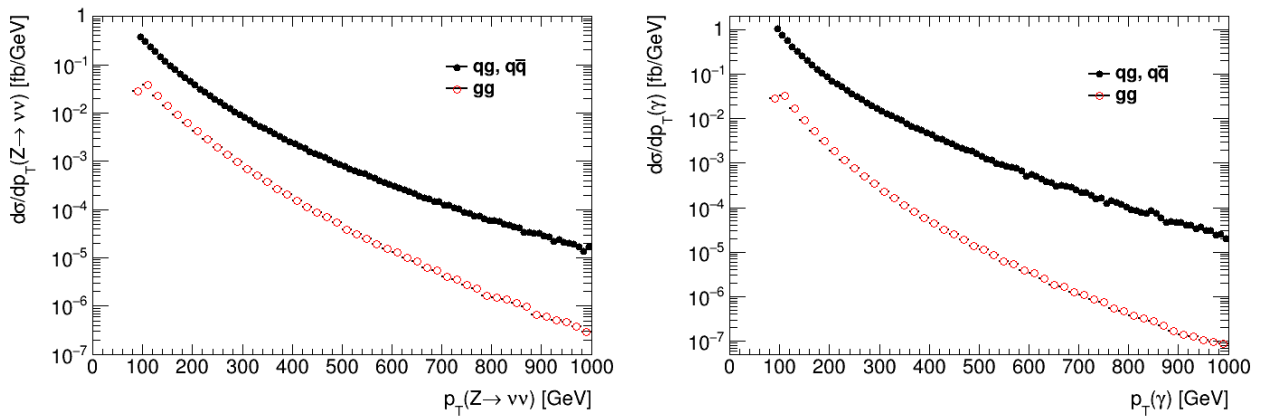
Figure 4.5: The cross sections of $ZZ \rightarrow ee\nu\nu$ (left) and $Z\gamma \rightarrow ee\gamma$ (right) as a function of p_T, from the contributing $q\bar{q}$, qg and gg processes. The leptonically decaying Z boson decays to an electron-positron pair

The R_{gg} distribution, shown in Figure 4.6 is observed to approach an asymptotic value at a much

higher $p_T = 2$ TeV. The gluon induced processes involve a box diagram, and understanding the behavior quantitatively is not as easy as it is for $q\bar{q}$ induced processes.
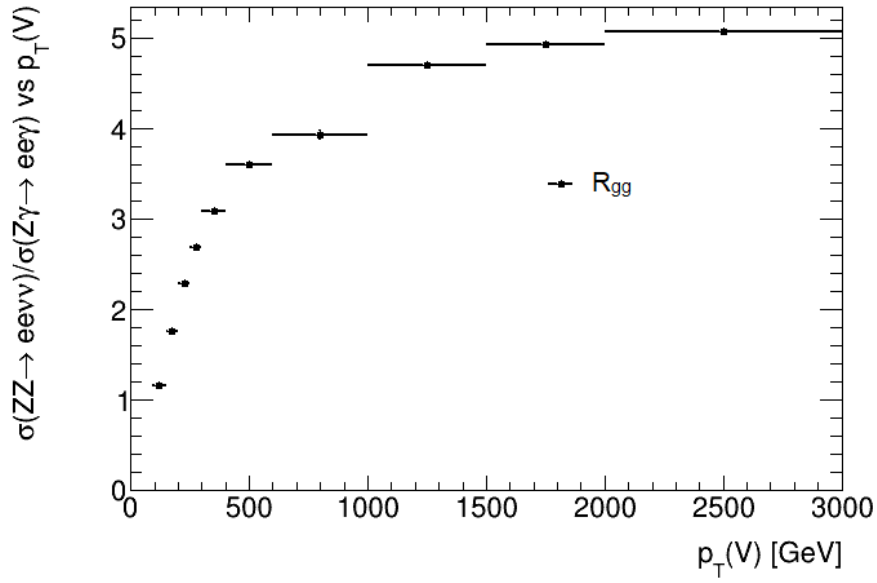
Figure 4.6: $R_{gg}(p_T)$, computed from the contributions of the gg subprocess to the cross sections of ZZ and $Z\gamma$. The curve reaches a plateau at a much higher p_T than for contributions from the $q\bar{q}$ process only. The leptonic Z bosons decay to an ee pair.

4.3 Theoretical Uncertainties

4.3.1 Uncertainty from Missing Higher Order Corrections

To address uncertainties associated with the scale in this study, a similar prescription as the one used in Ref [63] is followed. The central scale, μ_0 is chosen to be H_T for both $ZZ \to \ell\ell\nu\nu$ and $Z\gamma \to \ell\ell\gamma$ samples (where H_T is the scalar sum of the transverse momentum of all particles after collision, $\sum_i p_{T,i}$), and seven-point variations are applied, i.e.

$$\frac{\mu_i}{\mu_0} = (1,1),(1,2),(2,1),(2,2),(0.5,1),(1,0.5),(0.5,0.5) \tag{4.2}$$

where $i = 0,...,6$. The central cross section value is taken to be the mean of the maximum and minimum cross sections resulting from this variation, and the uncertainty to be the half the difference between the same.

$$\sigma_{NLO}^{(V)} = \frac{1}{2}\left[\sigma_{NLO}^{(V,max)} + \sigma_{NLO}^{(V,min)}\right] \tag{4.3}$$

$$\delta\sigma_{NLO}^{(V)} = \frac{1}{2}\left[\sigma_{NLO}^{(V,max)} - \sigma_{NLO}^{(V,min)}\right] \tag{4.4}$$

where

$$\sigma_{NLO}^{(V,max)} = max\left\{\sigma_{NLO}^{(V)}(p_T(V),\mu_i)|0 \le i \le 6\right\} \tag{4.5}$$

$$\sigma_{NLO}^{(V,min)} = min\left\{\sigma_{NLO}^{(V)}(p_T(V),\mu_i)|0 \le i \le 6\right\} \tag{4.6}$$

and $V = Z \to \nu\nu$ for $ZZ \to \ell\ell\nu\nu$, or $V = \gamma$ for $Z\gamma \to \ell\ell\gamma$. The value of R is calculated from the events generated with the above 7-point prescription in a correlated manner.

The variation of scales for cross sections of $ZZ \to ee\nu\nu$ and $Z\gamma \to ee\gamma$ are shown in Figure 4.7.

Figure 4.7: The scale variations around the cross sections of $ZZ \to ee\nu\nu$ (left) and $Z\gamma \to ee\gamma$ (right).

The uncertainty for $ZZ \to \ell\ell\nu\nu$ process is 2.5% at 100 GeV, which increases to 8.4% at high p_T. For the $Z\gamma \to \ell\ell\gamma$ process, the uncertainty increases from 3.5% at 100 GeV to 7.2% at high p_T. Here, the

prescription in Equations 4.3 and 4.4 is used to compute the central value and uncertainty.

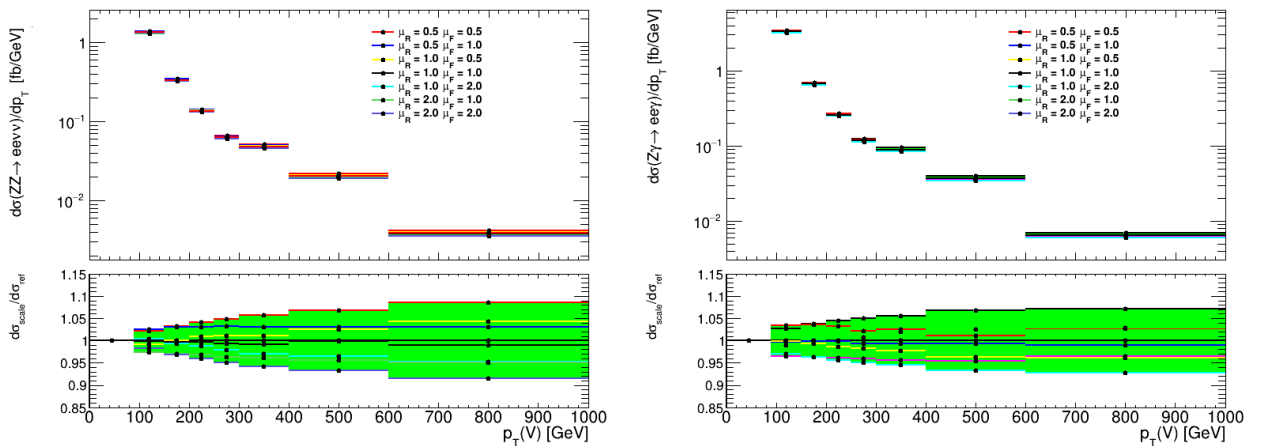Treating the scales as correlated between the processes, the scale variation for the transfer factor R is shown in Figure 4.8. The central value of R and the uncertainty band around it is taken according to Equations 4.3 and 4.4 applied to R.
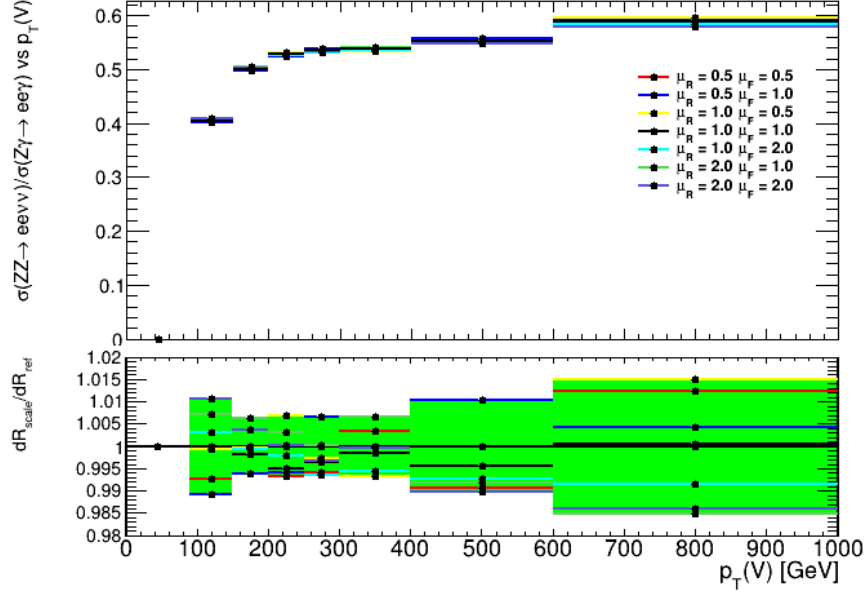
Figure 4.8: The transfer factor $R = \sigma(ZZ \to ee\nu\nu)/\sigma(Z\gamma \to ee\gamma)$ (top), with the scales varied in a correlated manner for both ZZ and $Z\gamma$ processes. The bottom plot shows the relative ratio R_i/R_0 of the varied transfer factors to the central value.

The correlated scale uncertainty around R is lower compared to that of the individual cross sections. At 100 GeV, $R \approx 0.404 \pm 0.004$, or an uncertainty of 1%. At $p_T = 500$ GeV, $R \approx 0.553 \pm 0.005$, the uncertainty is 1%, significantly lower than the large uncertainties ($\approx 8\%$) obtained for the individual cross sections at high p_T.

Varying the scales does not provide a complete picture of the missing higher order contributions. In going from LO to NLO, a significant difference is observed in the cross section prediction for both processes. To account for process dependent effects of QCD corrections at higher orders, we use the NLO K-factor, defined as the ratio of the cross section at NLO to the cross section at LO, as shown in equation 4.7.

$$K_{NLO}^{(V)} = \frac{\sigma_{NLO}^{(V)}}{\sigma_{LO}^{(V)}} \tag{4.7}$$

As seen in Figure 4.2a, the LO and NLO predictions for the transfer factor R agree quite well at high p_T, indicating that the K-factors for the $ZZ \to \ell\ell\nu\nu$ and $Z\gamma \to \ell\ell\gamma$ processes behave similarly in that regime, and that higher order QCD corrections are highly correlated between the two processes at high p_T. The difference between the K-factors of the two processes will be a measure of the difference in the contribution of higher order QCD corrections to them. This difference, δK_{NLO}, is taken as the K-factor uncertainty.

The following assumption is made regarding the NLO K-factor.

$$\frac{\sigma_{NLO}^{(V)}}{\sigma_{LO}^{(V)}} > \frac{\sigma_{N^\infty LO}^{(V)}}{\sigma_{NLO}^{(V)}} \tag{4.8}$$

35

It is also assumed that the *K*-factor difference at NLO is less than the *K*-factor difference at higher orders.

$$\left(\frac{\sigma_{NLO}^{(\gamma)}}{\sigma_{LO}^{(\gamma)}} - \frac{\sigma_{NLO}^{(Z)}}{\sigma_{LO}^{(Z)}} \right) < \left(\frac{\sigma_{N^{\infty}LO}^{(\gamma)}}{\sigma_{NLO}^{(\gamma)}} - \frac{\sigma_{N^{\infty}LO}^{(Z)}}{\sigma_{NLO}^{(Z)}} \right) \tag{4.9}$$

Figure 4.9 shows the *K*-factor distributions for both processes, as well as the *K*-factor uncertainty $\delta K_{NLO} = K_{NLO}^{(\gamma)}(p_T) - K_{NLO}^{(Z)}(p_T)$. The *K*-factor grows larger as a function of $p_T(V)$ for both processes. However, the difference between the two *K*-factors shrinks, due to the two processes being similar at high p_T.
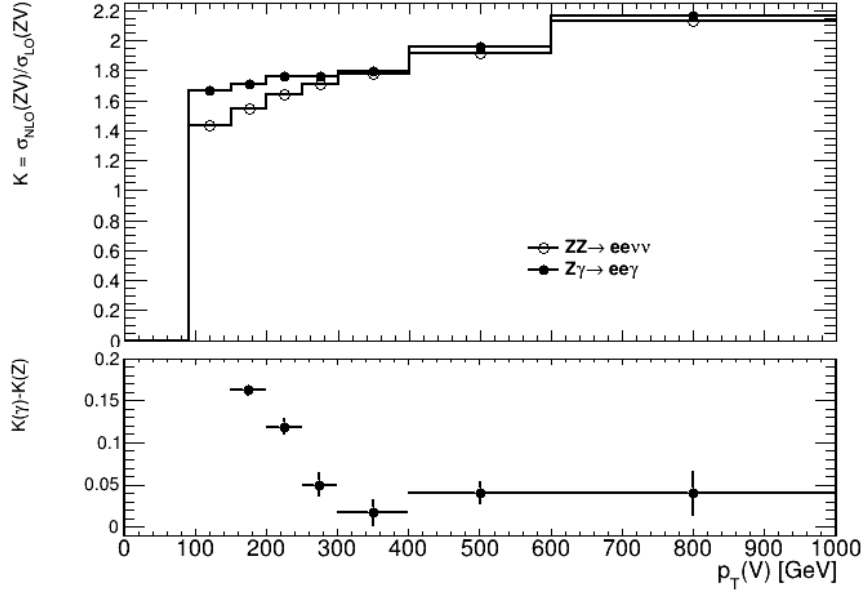
Figure 4.9: The *K* factor to estimate the unknown process dependent correlations, defined as $\sigma_{NLO}(V)/\sigma_{LO}(V)$. The bottom plot shows the difference between the *ZZ* and *Zγ* *K*-factors, δK_{NLO}, relative to *K(Z)*.

Thus, the *K*-factor uncertainty δK_{NLO}, is 4% at $p_T(V) = 500$ GeV. At low p_T the *K*-factors differ significantly between the two processes, e.g. at 100 GeV the difference is 23.6%

4.3.2 Uncertainty associated with Parton Distribution Functions

The PDF set used for reference is the `PDF4LHC15` [64] PDF set. The uncertainty on the PDFs is studied by using the 30 variations provided by the `PDF4LHC15` set [64], constructed from the combination of `CT14`,`MMHT14` and `NNPDF3.0` PDF sets. These sets are provided by LHAPDF6 [65]. `PDF4LHC15` provides a set of variations that include those determined by different groups (MSTW, CTEQ and NNPDF). The set used here is `PDF4LHC15_nlo_30`, consisting of 30 members.

Fig.4.10 shows the comparison of the ratio $R(p_T)$ from the 30 member sets of `PDF4LHC15_nlo_30`. To measure the uncertainty due to these 30 variations, analogous to Equation 20 in Ref [64], Equation 4.10 is used:

$$\delta^{PDF}R = \sqrt{\sum_{k=1}^{N_{mem}} (R^{(k)} - R^{(0)})^2} \tag{4.10}$$

where N_{mem} is the number of member sets in the group, in this case, 30.
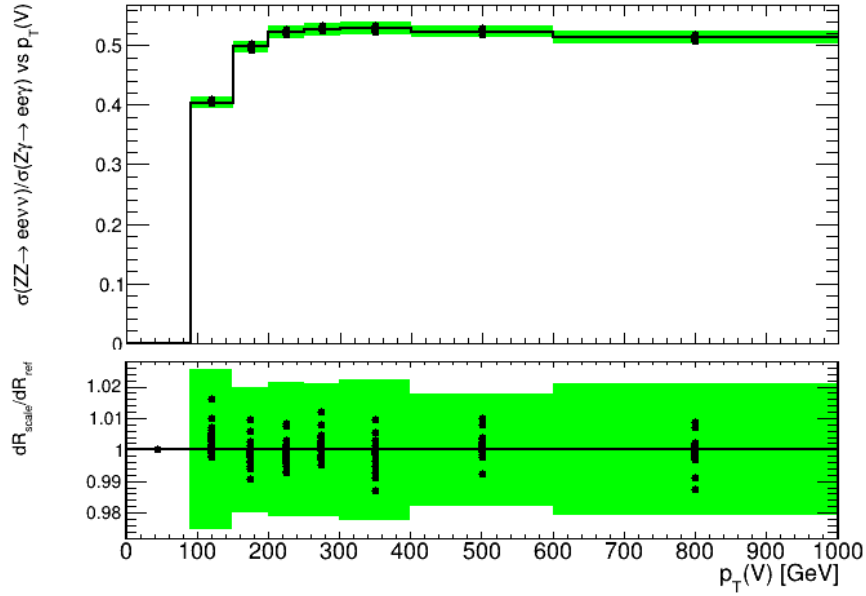
Figure 4.10: The transfer factor $R = \sigma(ZZ \to \ell\ell\nu\nu)/\sigma(Z\gamma \to \ell\ell\gamma)$ (top), and the relative ratio R_i/R_0 of the transfer factor calculated using PDF sets 1-30, with respect to set 0 which is taken as the central value.

The combined uncertainty around $R \approx 0.404$ is ± 0.010, or about 2.3%, at 100 GeV. The uncertainty is about 1.8% at high p_T values, with $R \approx 0.523 \pm 0.009$ at $p_T(V) = 500$ GeV.

4.3.3   Photon Fragmentation Uncertainty

To identify prompt photons, and separate them from photons that arise from showers or hadronic decay, it is necessary to isolate the photons from hadronic activity. Experimentally, photon isolation is implemented by limiting the hadronic energy in a cone around the photon to some fraction of the photon momentum. An alternative method is the smooth cone isolation, or the Frixione method which offers the advantage of avoiding fragmentation contributions and removing collinear singularities. Section 3.7 details these methods.

In this analysis, R_0 is chosen to be 0.4 to agree with the experimental definition. The two methods of photon isolation are very different. The central value is chosen to be from the sample using smooth cone isolation (Frixione) with $\varepsilon_h = 0.075$ and $n = 1$. These parameters are varied within a reasonable range to assess the uncertainty as shown in Figure 4.11. The parameters ε and n are varied to get a handle on the uncertainty associated with the Frixione isolation method. The experimental method of photon isolation is currently used in ATLAS analyses, and is therefore considered as well. The difference between the two different methods of isolation is expected to give a better handle on the uncertainties associated with the model of photon fragmentation.

37
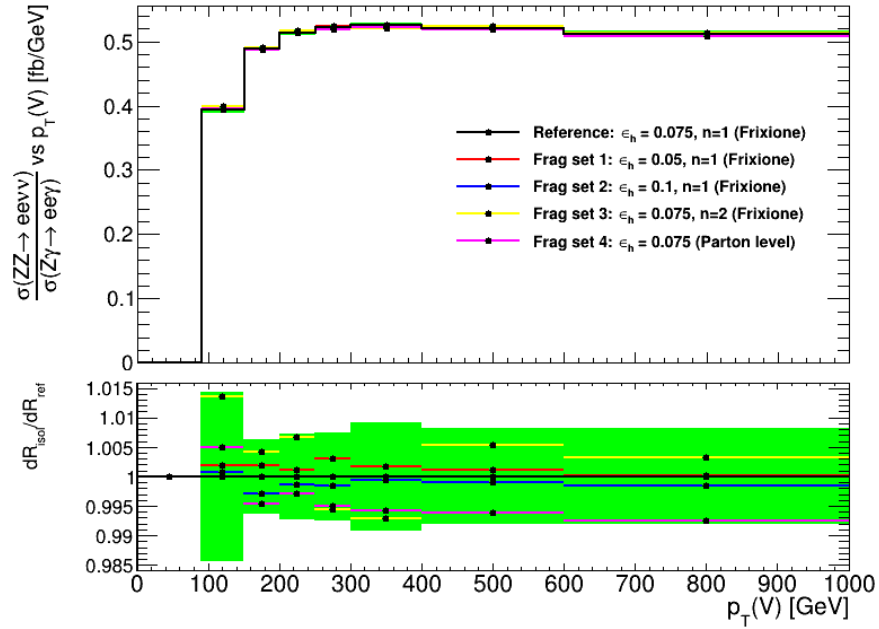
Figure 4.11: R distribution as a function of p_T, showing the uncertainty due to variation of photon isolation parameters ε_h and n in the smooth cone isolation procedure (Frixione), and ε_h in the photon isolation procedure. The lower panel shows the relative deviation of the varied sets from the central value, as well as the uncertainty band.

The uncertainty is calculated from the four sets listed in Figure 4.11:

$$\delta R_i = |R_i - R_{ref}| \qquad i \in (1,2,3,4)$$
$$\delta R = \sqrt{\max_{i=1,2,3}(\delta R_i)^2 + (\delta R_4)^2} \qquad (4.11)$$

as the effects assessed by changing the isolation definition in set 4, and varying the parameters in sets 1-3 are different.

The uncertainty is $< 1.5\%$ over the whole p_T range, and is 0.8% at $p_T(V) = 500$ GeV.

38

4.4 Combined Uncertainties

Combining the theoretical uncertainties due to missing higher order corrections, parton distribution functions, and photon fragmentation effects, Figure 4.12 shows the transfer factor R and its uncertainty.
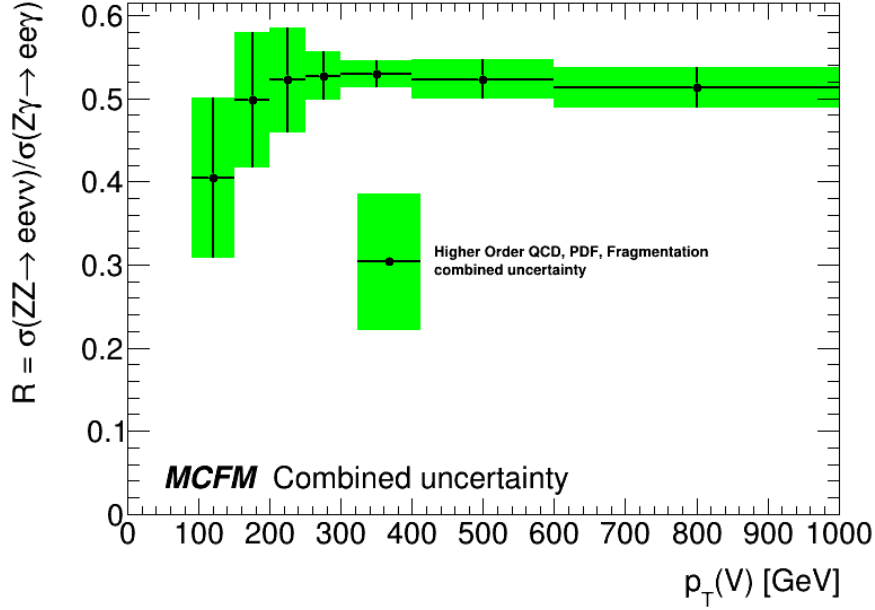
Figure 4.12: The transfer factor R with the combined theoretical uncertainties from missing higher order QCD corrections, parton distribution functions, and photon fragmentation effects.

The combined uncertainties are large at low p_T, with $R = 0.404 \pm 0.096 (23.8\%)$ at 100 GeV. However, the similarities in the $ZZ \rightarrow \ell\ell\nu\nu$ and $Z\gamma \rightarrow \ell\ell\gamma$ processes are apparent at high p_T, with $R = 0.523 \pm 0.024 (4.6\%)$ at 500 GeV.

Chapter 5

Conclusion

This thesis presents a method to estimate the Standard Model ZZ background to the $\ell\ell + E_T^{\text{miss}}$ final state in a Higgs to Dark Matter search.

Some BSM theories propose the Higgs boson as a mediator between Dark Matter and Standard Model particles. The Higgs boson is produced in association with a leptonically decaying Z boson, whereupon the Higgs boson decays into the invisible Dark Matter particles, resulting in a $\ell\ell + E_T^{\text{miss}}$ final state. This thesis estimates contribution of the $ZZ \rightarrow \ell\ell\nu\nu$ process to the Standard Model background in $\ell\ell + E_T^{\text{miss}}$ final state.

Estimated using Monte Carlo methods in Ref [53], an uncertainty of 10% was provided. This thesis summarizes the work on a data driven method using the $Z\gamma \rightarrow \ell\ell\gamma$ process to estimate the $ZZ \rightarrow \ell\ell\nu\nu$ contribution, as the two processes behave similarly at $p_T(V) \gg M_Z$; $V = Z \rightarrow \nu\nu$ or γ, i.e. the mass of the Z boson is negligible compared to its transverse momentum.

A transfer factor R is introduced as the ratio of the $ZZ \rightarrow \ell\ell\nu\nu$ cross section to the $Z\gamma \rightarrow \ell\ell\gamma$ cross section, and the theoretical uncertainties upon R are estimated. The uncertainties due to missing higher order corrections are 23.6% at $p_T(V) = 100$ GeV and 4.1% at $p_T(V) = 500$ GeV. Uncertainties due to parton distribution functions are 2.3% at 100 GeV, and 1.8% at 500 GeV. The uncertainties due to photon fragmentation effects are $< 1.5\%$ in the full p_T range considered, and 0.8% at 500 GeV.

The combined uncertainties are large at low p_T, 23.8%, at 100 GeV, but are small at high p_T, 4.6% at 500 GeV. While at low p_T, the uncertainty obtained is inferior than the 10% uncertainty for the ZZ background obtained from $ZH \rightarrow \ell\ell + E_T^{\text{miss}}$ search, the uncertainty is reduced by a factor of 2 at high p_T. Thus, the transfer factor R can be used on $Z\gamma \rightarrow \ell\ell\gamma$ data to estimate the contribution of $ZZ \rightarrow \ell\ell\nu\nu$.

5.1 Outlook

This study was conducted at NLO using MCFM, a matrix element generator. Further studies are being conducted to reproduce these results and improve the uncertainty estimates by repeating the measurements at NNLO using MATRIX [66]. It is also necessary to account for detector effects and estimate experimental uncertainties, which will be conducted with Monte Carlo techiniques with the ATLAS framework. These studies are in progress, and are not within the scope of this thesis.

Bibliography

[1] D.J. Griffiths, *Introduction to Elementary Particles 2nd Edition*, 2004 WILEY-VCH Verlag GmbH & Co. KGaA, Weinheim

[2] PBS NOVA, Fermilab, Office of Science, United States Department of Energy, Particle Data Group.

[3] Richard Feynman, *QED: The Strange Theory of Light and Matter*, Princeton University Press, 1986.

[4] J. Greensite, *An introduction to the confinement problem*, Springer 2011, ISBN 978-3-642-14382-3

[5] The Super-Kamiokande Collaboration, *Evidence for oscillations of atmospheric neutrinos*, Phys.Rev.Lett.81:1562-1567, 1998, `arXiv:hep-ex/9807003`

[6] The SNO Collaboration, *Measurement of the rate of $\nu_e + d \rightarrow p + p + e^-$ interactions produced by ^8B solar neutrinos at the Sudbury Neutrino Observatory*, Phys.Rev.Lett.87:071301,2001, `arXiv:nucl-ex/0106015`

[7] The SNO Collaboration, *Direct Evidence for Neutrino Flavor Transformation from Neutral-Current Interactions in the Sudbury Neutrino Observatory*, Phys.Rev.Lett.89:011301,2002, `arXiv:nucl-ex/0204008`

[8] F. Halzen, A. Martin, *Quarks and Leptons: An introductory course in model particle physics*, John Wiley and Sons, 1984.

[9] J. H. Christenson, J. W. Cronin, V. L. Fitch, and R. Turlay, *Evidence for the 2π Decay of the K_2^0 Meson, Phys. Rev. Lett. 13, 138 (1964)*, Decay of the K_2^0 Meson, Phys. Rev. Lett. 13, 138 (1964), `https://doi.org/10.1103/PhysRevLett.13.138`

[10] M. Kobayashi T. Maskawa, *CP-Violation in the Renormalizable Theory of Weak Interaction, Progress of Theoretical Physics*, Volume 49, Issue 2, 1 February 1973, 652–657, `https://doi.org/10.1143/PTP.49.652`

[11] KTEV Collaboration, *Observation of Direct CP Violation in $K_{S,L} \rightarrow \pi\pi$ Decays*, Phys.Rev.Lett.83:22-27,1999, `arXiv:hep-ex/9905060`

[12] NA48 Collaboration, *A new measurement of direct CP violation in two pion decays of the neutral kaon*, Phys.Lett.B465:335-348,1999, `arXiv:hep-ex/9909022`

[13] BaBar collaboration, *Measurement of CP-violating asymmetries in B^0 decays to CP eigenstates*, Phys.Rev.Lett.86:2515-2522,2001, `arXiv:hep-ex/0102030`

[14] Belle Collaboration, *Observation of Large CP Violation in the Neutral B Meson System*, Phys.Rev.Lett.87:091802,2001, `arXiv:hep-ex/0107061`

[15] LHCb Collaboration, *Measurement of CP asymmetry in $D^0 \to K^+K^-$ and $D^0 \to \pi^+\pi^-$ decays*, JHEP 07 (2014) 041, `arXiv:1405.2797 [hep-ex]`

[16] LHCb Collaboration, *First observation of CP violation in the decays of B_s^0 mesons*, Phys. Rev. Lett. 110 (2013) 221601, `arXiv:1304.6173 [hep-ex]`

[17] ATLAS Collaboration, *Observation of a New Particle in the Search for the Standard Model Higgs boson with the ATLAS detector at the LHC*, Phys.Lett. B716 (2012) 1-29, `arXiv:1207.7214 [hep-ex]`

[18] The CMS Collaboration, *Observation of a new boson at a mass of 125 GeV with the CMS experiment at the LHC*, Phys. Lett. B 716 (2012) 30, `arXiv:1207.7235 [hep-ex]`

[19] Jaco de Swart, Gianfranco Bertone, Jeroen van Dongen, *How Dark Matter came to matter*, Nature Astronomy 1, 0059 (2017), `arXiv:1703.00013 [astro-ph.CO]`

[20] P. J. E. Peebles, Bharat Ratra, *The Cosmological Constant and Dark Energy (2002)*, Rev.Mod.Phys.75:559-606,2003, `arXiv:astro-ph/0207347`

[21] Planck Collaboration, *Planck 2015 results. XIII. Cosmological parameters (2016)*, A&A 594, A13 (2016), `arXiv:1502.01589 [astro-ph.CO]`

[22] N. Jarosik et al., *Seven-Year Wilkinson Microwave Anisotropy Probe (WMAP) Observations: Sky Maps, Systematic Errors and Basic Results*, Astrophys. J. Suppl. 192 14 (2011) [1001.4744], `arXiv:1001.4744 [astro-ph.CO]`

[23] S. Weinberg, *Implications of Dynamical Symmetry Breaking*, Phys. Rev. D13 (1976) 974–996, `https://doi.org/10.1103/PhysRevD.13.974`

[24] S. Weinberg, *Implications of Dynamical Symmetry Breaking: An Addendum*, Phys. Rev. D19 (1979) 1277–1280, `https://doi.org/10.1103/PhysRevD.19.1277`

[25] L. Susskind, *Dynamics of spontaneous symmetry breaking in the Weinberg-Salam theory*, Phys. Rev. D20 (1979) 2619–2625, `https://doi.org/10.1103/PhysRevD.20.2619`

[26] E. Gildener, *Gauge Symmetry Hierarchies*, Phys. Rev. D14(1976) 1667, `https://doi.org/10.1103/PhysRevD.14.1667`

[27] Laurent Canetti, Marco Drewes, Mikhail Shaposhnikov, *Matter and Antimatter in the Universe*, New J. Phys. 14 (2012) 095012, `arXiv:1204.4186 [hep-ph]`

[28] M.C.Gonzalez-Garcia, Michele Maltoni, *Phenomenology with Massive Neutrinos*, Phys.Rept.460:1-129,2008, `arXiv:0704.1800 [hep-ph]`

[29] Vernon Barger, Danny Marfatia, Kerry Lewis Whisnant, *The Physics of Neutrinos (2012)*, Princeton University Press, ISBN 0-691-12853-7

[30] A. O. Sushkov, W. J. Kim, D. A. R. Dalvit, S. K. Lamoreaux, *New experimental limits on non-Newtonian forces in the micrometer-range*, Phys. Rev. Lett. 107, 171101 (2011), `arXiv:1108.2547 [quant-ph]`

[31] Begeman, K. G., Broeils, A. H., Sanders, R. H., *Extended rotation curves of spiral galaxies - Dark haloes and modified dynamics*, Monthly Notices of the Royal Astronomical Society (ISSN 0035-8711), vol. 249, April 1, 1991, p. 523-537.

[32] Felix Kalhoefer, *Review of LHC Dark Matter searches*, Int.J.Mod.Phys. A32 (2017) 1730006, `arXiv:1702.0243 [hep-ph]`

[33] Philip Harris, Valentin V. Khoze, Michael Spannowsky, Ciaran Williams, *Closing up on Dark Sectors at Colliders: from 14 to 100 TeV*, Phys. Rev. D 93, 054030 (2016), `arXiv:1509.02904 [hep-ph]`

[34] Jing-Yuan, Edward W. Kolb, Lian-Tao Wang, *Dark matter coupling to electroweak gauge and Higgs bosons: an effective field theory approach*, Phys.Dark Univ. 2 (2013) 200-218, `arXiv:1305.0021 [hep-ph]`

[35] ATLAS Collaboration, *Search for dark matter produced in association with a Higgs boson decaying to two bottom quarks in pp collisions at $\sqrt{s} = 8$ TeV with the ATLAS detector*, Phys. Rev. D 93, 072007 (2016), `arXiv:1510.06218 [hep-ex]`

[36] Rende Steerenberg, Stefania Pandolfi, *LHC report: full house for the LHC*, `http://cds.cern.ch/record/2272573`

[37] V. Barger, R. Phillips, *Collider Physics (Frontiers in Physics)*, Avalon Publishing, 1997.

[38] R. K. Ellis, W. J. Stirling, and B. R. Webber, *QCD and Collider Physics*, Cambridge Monographs, 2003

[39] A.D. Martin, W.J. Stirling, R.S. Thorne, G. Watt, *Parton distributions for the LHC*, Eur.Phys.J.C63:189-285,2009, `arXiv:0901.0002 [hep-ph]`

[40] A.D. Martin, W.J. Stirling, R.S. Thorne, G. Watt, *Uncertainties on α_s in global PDF analyses and implications for predicted hadronic cross sections*, Eur.Phys.J.C64:653-680,2009, `arXiv:0905.3531 [hep-ph]`

[41] A.D. Martin, W.J. Stirling, R.S. Thorne, G. Watt, *Heavy-quark mass dependence in global PDF analyses and 3- and 4-flavor parton distributions*, Eur.Phys.J.C70:51-72,2010, `arXiv:1007.2624 [hep-ph]`

[42] L. A. Harland-Lang, A. D. Martin, P. Motylinski, R. S. Thorne, *Parton distributions in the LHC era: MMHT 2014 PDFs*, Eur. Phys. J. C (2015) 75: 204, `arXiv:1412.3989 [hep-ph]`

[43] The NNPDF collaboration, *Parton distributions for the LHC Run II*, J. High Energ. Phys. (2015) 2015: 40, `arXiv:1410.8849 [hep-ph]`

[44] The ATLAS Collaboration et al, *The ATLAS experiment at the CERN Large Hadron Collider*, 2008 JINST 3 S08003, `https://doi.org/10.1088/1748-0221/3/08/S08003`

[45] Heather M Gray, *Alignment of the ATLAS inner detector tracking system*, 2009 JINST 4 P03018, `https://doi.org/10.1088/1748-0221/4/03/P03018`

[46] N Garelli and the Atlas Collaboration, *The Evolution of the Trigger and Data Acquisition System in the ATLAS Experiment*, 2014 J. Phys.: Conf. Ser. 513 012007, `https://doi.org/10.1088/1742-6596/513/1/012007`

[47] A Negri, *Evolution of the Trigger and Data Acquisition System for the ATLAS experiment*, 2012 J. Phys.: Conf. Ser. 396 012033, `https://doi.org/10.1088/1742-6596/396/1/012033`

[48] The ATLAS Collaboration, *ATLAS high-level trigger, data-acquisition and controls : Technical Design Report*, ATLAS-TDR-16 ; CERN-LHCC-2003-022

[49] B. Abbott et al, *The evolution of the region of interest builder for the ATLAS experiment at CERN*, 2016 JINST 11 C02080, `https://doi.org/10.1088/1748-0221/11/02/C02080`

[50] Alwall, J., Frederix, R., Frixione, S. et al., *The automated computation of tree-level and next-to-leading order differential cross sections, and their matching to parton shower simulations*, J. High Energ. Phys. (2014) 2014: 79, `arXiv:1405.0301 [hep-ph]`

[51] T. Sjöstrand, S. Mrenna and P. Skands, *PYTHIA 8.1*, JHEP05 (2006) 026, Comput. Phys. Comm. 178 (2008) 852

[52] Geant4 Collaboration, S.Agostinelli et. al., *Geant4—a simulation toolkit*, Nucl. Instrum. Meth. A 506 (2003) 250–303, `https://doi.org/10.1016/S0168-9002(03)01368-8`

[53] ATLAS Collaboration, *Search for an invisibly decaying Higgs boson or dark matter candidates produced in association with a Z boson in pp collisions at $\sqrt{s}$ = 13 TeV with the ATLAS detector*, PLB 776 (2017), 318, `arXiv:1708.09624 [hep-ex]`

[54] S. Ask, M. A. Parker, T. Sandoval, M. E. Shea, W. J. Stirling, *Using γ+ jets to calibrate the Standard Model $Z(\to \nu\nu)$+ jets background to new processes at the LHC*, J. High Energ. Phys. (2011) 2011: 58, `arXiv:1107.2803 [hep-ph]`

[55] C. Patrignani *et al.* (Particle Data Group), *2017 Review of Particle Physics - Particle Listings*, Chin. Phys. C, 40, 100001 (2016)

[56] Tung-Mow Yan, Sidney D. Drell, *The Parton Model and its Applications*, Int. J. Mod. Phys. A 29, 1430071 (2014), arXiv:1409.0051 [hep-ph]

[57] W. Pauli and F. Villars, *On the Invariant Regularization in Relativistic Quantum Theory*, Rev. Mod. Phys. 21, 434 (1949), `https://doi.org/10.1103/RevModPhys.21.434`

[58] S. Frixione, *Isolated photons in perturbative QCD*, Phys.Lett. B429 (1998) 369-374, `arXiv:hep-ph/9801442`

[59] J. Campbell, K. Ellis, *An update on vector boson pair production at hadron colliders*, Phys. Rev. D60, 113006 (1999), arXiv:hep-ph/9905386

[60] J. M. Campbell, R. K. Ellis and C. Williams, *Vector boson pair production at the LHC, JHEP 1107, 018 (2011),*, arXiv:1105.0020 [hep-ph]

[61] J. M. Campbell, R. K. Ellis and W. Giele, *A Multi-threaded Version of MCFM*, EPJ C75, 246 (2015), arXiv:1503.06182 [physics.comp-ph]

[62] John Campbell, Keith Ellis, Walter Giele, Ciaran Williams, *Monte Carlo for FeMtobarn processes (MCFM) v8.0 User Manual*, `https://mcfm.fnal.gov/`

[63] J.M. Lindert, S. Pozzorini, et al., *Precise predictions for V +jets dark matter backgrounds*, Eur. Phys. J. C (2017) 77: 829 `arXiv:1705.04664 [hep-ph]`

[64] Jon Butterworth, Stefano Carrazza, et al, *PDF4LHC recommendations for LHC Run II*, J. Phys. G: Nucl. Part. Phys. 43 023001 (2016), `arXiv:1510.03865 [hep-ph]`

[65] Buckley, A., Ferrando, J., Lloyd, S. et al., *LHAPDF6: parton density access in the LHC precision era*, Eur. Phys. J. C (2015) 75: 132, `arXiv:1412.7420 [hep-ph]`

[66] Massimiliano Grazzini, Stefan Kallweit, Marius Wiesemann, *Fully differential NNLO computations with MATRIX*, CERN-TH-2017-232, ZU-TH 30/17, `arXiv:1711.06631 [hep-ph]`

46